Review

A review on structural characteristics and thermoelectric properties of mid-temperature range Chalcogenide-based thermoelectric materials

Manasa R. Shankar[1], and A. N. Prabhu[1,*] (ID)

[1] *Department of Physics, Manipal Institute of Technology, Manipal Academy of Higher Education, Manipal 576104, India*

ABSTRACT

Several affordable and pollution-free technologies have drawn a lot of attention because of the pressure of our energy needs and environmental problems; among these, thermoelectric technology has made enormous advances. It has been known that thermoelectric materials are efficient in transforming waste heat energy into electricity. The efficiency of thermoelectric materials is typically assessed using the ZT value, $ZT = S^2T/\varrho\kappa$. Several methods have been highlighted in the literature for improving thermoelectric figure of merit. This review stands out for its particular emphasis on cutting-edge techniques that are leading to a new era of thermoelectric innovation, including doping, co-doping, alloying, nanostructuring, and nanocompositing. Our focus is on mid-temperature range thermoelectric materials, which operate between 500 and 900 K and have enormous potential for high-efficiency thermoelectricity and waste heat recovery due to their inherent thermal and electrical properties. This review provides a foundational understanding of thermoelectric concepts as well as obstacles to improving the figure of merit and the various classes of mid-temperature range thermoelectric materials, including their structure and thermoelectric characteristics are discussed in brief. Additionally, it also discusses different methods described in the various literature regarding enhancing performance as well as recent advancements made in this area and this article emphasizes the relevance and importance of these developments in the context of urgent global energy challenges and highlights the crucial role that mid-temperature range thermoelectric materials will play in determining the future landscape of sustainable energy sources. To satisfy the practical demand, scientific research in the field of thermoelectricity still needs to be intensified, for this mid-temperature range, Chalcogenide-based thermoelectric materials play a very important role in the future.

GRAPHICAL ABSTRACT
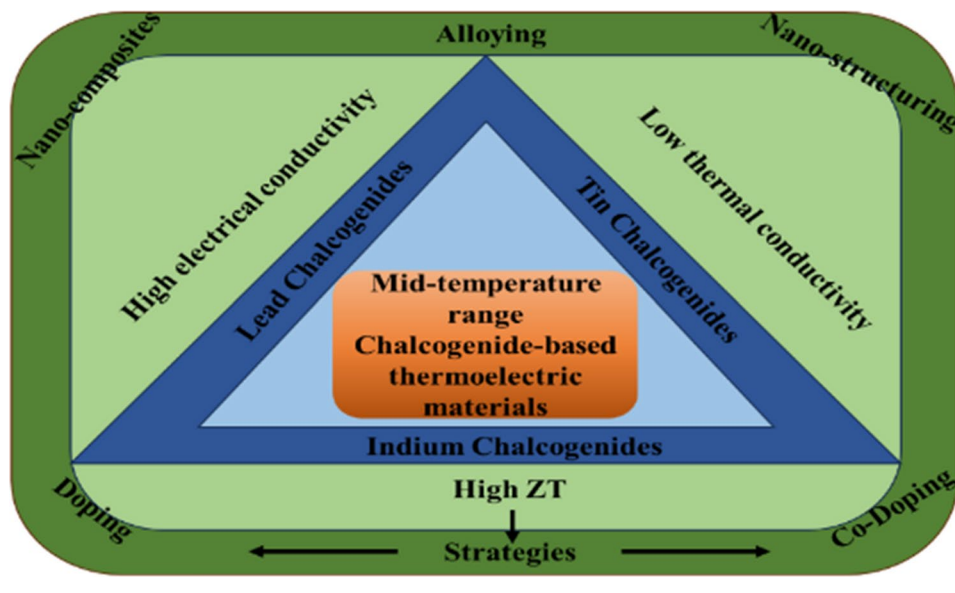
Introduction

Our society mainly depends on energy to maintain our living standards and to serve all other components of our economy [1]. Energy consumption has increased dramatically in recent years. This demand is primarily met by the burning of fossil fuels, and coal, which ultimately resulted in the release of greenhouse gases. Due to the declining reserves of fossil fuels along with the bad impacts of the emission of greenhouse gases on the environment [2], to tackle this issue, the world is striving for clean, affordable, and long-lasting energy by utilizing renewable forms of energy like wind, solar, biomass and tidal. Realizing that a major portion of the energy we consume is lost as heat, hence, this waste heat can be converted into a beneficial form of energy like electricity. Thermoelectric materials are one such kind of material having the potential to convert heat energy into electricity and reverse [3]. Thermoelectric devices have attracted the research community over other technologies by their unique properties like toxic-free action, immovable parts, and no chemical reactions during the process [1].

The majority of heat is wasted in industries, power plants, and automobiles. We can utilize this heat and it can be converted into a useful form of energy by using mid-temperature range thermoelectric materials. The major drawback of these materials/devices is their poor efficiency, because of low ZT values, which restricts their use at the commercial level. If the efficiency of these materials improved significantly, then thermoelectric devices could play an important role in addressing today's energy challenges. But efficiency optimization is a great challenge, as a result, the main question in this field of research is how to increase thermoelectric efficiency in these materials.

The principal purpose of this review is to provide a broad analysis of the structural properties and synthetic strategies of mid-temperature range Chalcogenide-based thermoelectric materials, as well as recent research on strengthening their figure of merit. This review initially discusses the fundamentals of thermoelectric materials, various types of thermoelectric materials based on its working temperature, and dimensionless figure of merit. The detailed discussion of mid-temperature Chalcogenide-based thermoelectric materials follows a general outline of their structure and thermoelectric characteristics. The impact of various mechanisms utilized in the literature to boost their ZT is also evaluated. This review focuses to provide some information on the energy conversion applications of mid-temperature Chalcogenide-based thermoelectric materials by underlining the obstacles and possibilities in the evolution of these materials.

Fundamental theory of thermoelectrics

Fundamentally the thermoelectric effect is the process of temperature differences being directly converted to electric voltage and vice versa [4]. Thermoelectric effect mainly consists of three main effects those are.

- Seebeck effect
- Peltier effect
- Thomson effect

Thermoelectrics seems to be an old concept because the Seebeck effect introduced by the German physicist Thomas Johann Seebeck in 1821, states that when a thermocouple is exposed to a temperature gradient, it creates voltage. This is known as the Seebeck effect and the schematic representation of the Seebeck effect is shown in Fig. 1a [4, 5]. This effect is mathematically described by Eq. 1,

$$\Delta V = S\Delta T \tag{1}$$

where S is the Seebeck coefficient, ΔT is the temperature difference, and ΔV is the thermoelectric potential [4].

The second effect under the thermoelectric effect is the Peltier effect, which states that thermoelectric devices have the potential to convert electrical energy into a temperature gradient, this was first recognized by Peltier in 1834 [5]. Figure 1b shows the schematic diagram of the Peltier effect. The amount of current control and how gradually heat(Q) is released or absorbed at a thermocouple junction and this is mathematically represented by Eq. 2.

$$\frac{dQ}{dt} = \Pi i \tag{2}$$

where Π is the Peltier coefficient [6].

The third effect under the thermoelectric effect is the Thomson effect, which states that when applying electrical current(I) to a single conducting material with a temperature difference between two endpoints, the material will either eject or absorb heat [7] this was first recognized by William Thomson. Figure 1c shows the schematic diagram of the Thomson effect. The Thomson coefficient is mathematically represented by Eq. 3.

$$\beta = \frac{Q}{I\Delta T} \tag{3}$$

where β is the Thomson coefficient.

Kinds of thermoelectric materials

The materials which follow the above effects (Seebeck, Peltier, Thomson) are called thermoelectric materials. Thermoelectric materials are classified into three main categories based on their working temperatures, namely (i) Low-temperature thermoelectric materials, (ii) Mid-temperature thermoelectric materials, and (iii) High-temperature thermoelectric materials [8].

i) Low-temperature thermoelectric materials: These are the materials whose working temperature is less than 500 K and are also called near-room temperature thermoelectric materials. Tetradymites, alloys like Bismuth Chalcogenides (Bi_2Se_3 [9], Bi_2Te_3 [10], Bi_2S_3 [11]), and Antimony Chalcogenides (Sb_2Se_3 [12], Sb_2Te_3 [13], Sb_2S_3 [14]) belong to the family of low-temperature thermoelectric materials.

ii)Mid-temperature thermoelectric materials: These are the materials whose working temperature lies between 500 and 900 K. Lead Chalcogenides (PbTe [15], PbSe [16], PbS [17]), Tin Chalcogenides (SnSe [18], SnTe [19], SnS [20]), Indium Chalcogenides (InSe [21], InTe [22], InS [23]), and Germanium Chalcogenides
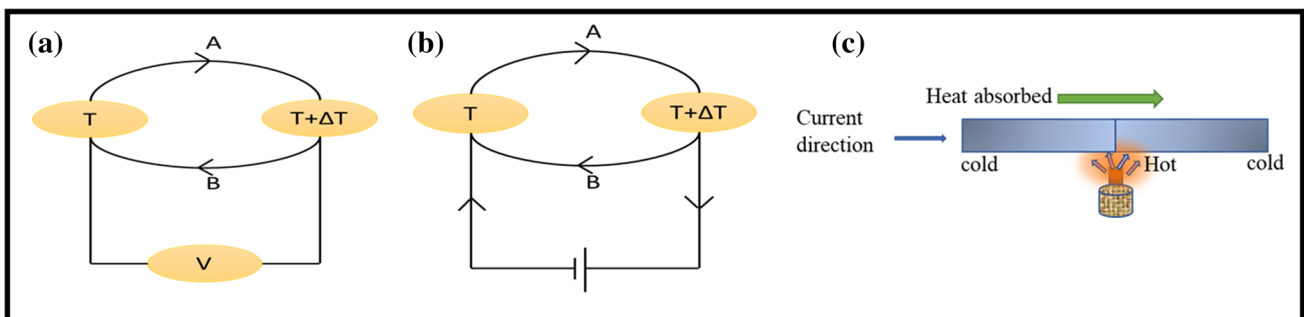

Figure 1 The Schematic diagram of the **a** Seebeck effect **b** Peltier effect **c** Thomson effect.

(GeTe [24], GeSe [25], GeS [26]) and many more belong to the group of mid-temperature range thermoelectric materials.

iii) High-temperature thermoelectric materials: These are the materials whose working temperature is greater than 900 K. SiGe [27], La_3Te_4 [28], $Yb_{14}MnSb_{11}$ [29], ZrNiSn-, and FeNbSb-based [30] half-Heusler alloys belong to high-temperature thermoelectric materials [31].

Among these three major classifications, this review mainly focused on structure, synthesis techniques, efficiency, drawbacks, and applications of mid-temperature thermoelectric material.

The mid-temperature range chalcogenide-based TE materials have a wide range of potential applications, particularly in energy harvesting and efficiency enhancement across various industries, portable power generation, aerospace and space exploration, automotives, medical devices etc.

Thermoelectric efficiency

David Rowe, a physicist at the National Renewable Energy Laboratory, was the person who first introduced the idea of ZT as a measurement of thermoelectric efficiency in the middle of the 1980s. Prior to the invention of ZT, initially, in the early 90's the figure-of-merit is represented by 'Z' and the unit used is per kelvin [32], afterward to make this quantity dimensionless it changed to ZT. The temperature of the material, which is a crucial factor in determining its efficiency, was not considered in this measure before the 90 s. Since its introduction in Z makes it as ZT, takes temperature into account while calculating thermoelectric efficiency, has become the benchmark for assessing and contrasting the performance of various thermoelectric materials. The conversion efficiency of heat into a useful form of energy of thermoelectric materials mainly depends on the dimensionless figure-of-merit (ZT) and the ZT is represented by Eq. 4 [33].

$$ZT = \frac{S^2 T}{\rho k} \qquad (4)$$

where S is the Seebeck coefficient, ρ is electrical resistivity, T is absolute temperature, and $k = k_{electronic} + k_{lattice}$ is total thermal conductivity due to electronic and lattice thermal conductivity [34]. All these parameters are interdependent on one another. Hence, the optimization of one parameter leads to

changes in the other. Therefore, this stands as the uppermost challenge to increase efficiency in thermoelectric materials. Enhancing ZT in the typical medium temperature material involve some mechanisms like 1. Electrical Transport Optimization: Electrical Conductivity (σ): Increasing σ by doping or alloying to enhance the material's ability to conduct electricity efficiently, Seebeck Coefficient (S): Raising the Seebeck coefficient to maximize voltage generation when a temperature gradient is applied. This is achieved through band engineering of the material's electronic structure. Together, high σ and S contribute to a high power factor, a critical factor for ZT improvement. 2. Reduction of Thermal Conductivity (κ): To boost ZT, it is essential to reduce thermal conductivity. Lower κ minimizes heat loss and is achieved through various mechanisms like phonon scattering: Introducing structural defects, nanostructuring of the material, or creating alloyed structures to scatter phonons effectively, thereby hindering their ability to transport heat. Boundary Effects: Capitalizing on grain boundaries, interfaces, and other structural features to impede phonon heat transfer. Interfaces of this type can serve as phonon scattering sites for lowering thermal conductivity. 3. Band Structure Engineering: Medium-temperature thermoelectric materials often undergo band structure engineering. This involves modifying the electronic band structure to influence the transport of both charge carriers (electrons or holes) and phonons. Tailoring Bandgap: Adjust the bandgap to match the energy levels of carriers in the operating temperature range. A suitable bandgap ensures efficient charge transport without excessive heat generation. Effective Mass Engineering: Modifying the effective mass of charge carriers can significantly impact their mobility and, consequently, their electrical conductivity. Energy Filtering: Restructuring the band edges to enhance the Seebeck coefficient. This can be achieved by manipulating the density of states in the energy range of interest. 4. Phonon Engineering: Phonons are responsible for heat conduction in solids. Therefore, phonon engineering strategies aim to limit phonon transport by introducing structural complexities, such as nanostructures or super lattices and by employing materials with strong phonon scattering characteristics. Two notable theoretical models utilized for band structure analysis are the single parabolic band (SPB) model and the Kane Band (KB) model. These models help in understanding and engineering the electronic properties of thermoelectric materials to optimize their

ZT values and theoretical calculations based on first-principles density functional theory (DFT) [35] have become indispensable tools in the design and evaluation of thermoelectric materials. DFT enables researchers to predict electronic structure, phonon dispersion, and defect formation energies accurately. Both the Kane band (KB) model and the single parabolic band (SPB) model can be used to investigate the n- or p-dependent ZT. The correlation between n or p and ZT for different thermoelectric materials is frequently investigated using conventional first-principles density functional theory (DFT) calculations [5].

Structure of mid-temperature thermoelectric materials

Lead Chalcogenide series

Lead chalcogenides are a class of materials that contain both metal and chalcogen elements. Chalcogenide compounds are made up of three key elements: sulfur, selenium, and tellurium PbX (X = S, Se, Te), these have gained considerable attention with a narrow band gap, outstanding and tunable electronic transport properties, and low thermal conductivity [36] (Fig. 2).

Lead telluride (PbTe)

Figure 3a shows a binary phase diagram of Pb-Te, it illustrates the temperature and stoichiometric

composition dependence of the crystal structure of different phases, which is important in figuring out the physical and chemical properties of these materials. According to the binary phase diagram of lead telluride (PbTe), a 50–50 composition of lead (Pb) and tellurium (Te) would correspond to the eutectic composition. Lead telluride exists in only one phase, which is the PbTe phase at 50–50 atomic percentages of lead and tellurium. At this composition, a eutectic mixture or a eutectic phase will form. Lead telluride is categorized as a mid-temperature thermoelectric material. It can work at a maximum temperature of 900 K. In addition to its excellent figure of merit, PbTe has a high melting point, superior chemical stability, low vapor pressure, and good chemical Stability [42]. The structure of lead telluride, PbTe, is rock salt (face-centered cubic (FCC)) with Fm3m space group and the lattice constant a = 6.460 Å. As a result of stoichiometric deviation, PbTe can be n- or p-type (if Pb-rich PbTe is n-type, while Te-rich PbTe is p-type) [43]. It crystallizes as NaCl, with Pb atoms occupying the cation and Te forming the anionic lattice with a narrow band gap at an L point (a specific high symmetry point in the Brillouin zone of a crystal lattice) of 0.32 eV [44]. The PbTe structure is composed of two interlayer fcc lattices, one of Pb atoms and the other of Te atoms bonded by combined ionic and covalent bonds. As shown in Fig. 2a, each atom is octahedrally coordinated by the six nearest neighbors of the other type [45] and Fig. 4a–c shows the TEM images of PbTe compound, which shows the cubic structure of the compound.
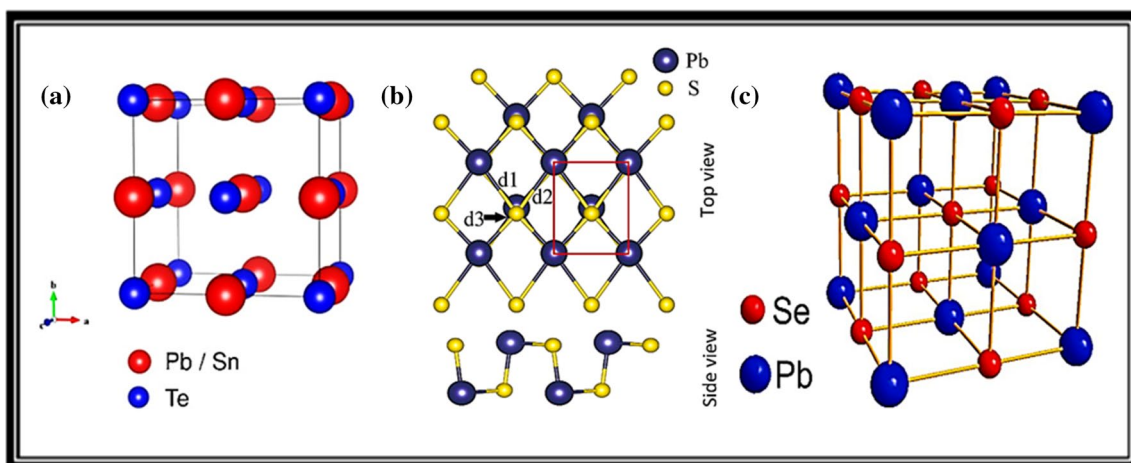

Figure 2 Crystal structure models of **a** PbTe reproduce with permission [37], copyright 2012, John Wiley and Sons. **b** PbS reproduced with permission [38]. Copyright 2021, Elsevier. **c** PbSe reproduced with permission [39]. Copyright 2022, Elsevier.
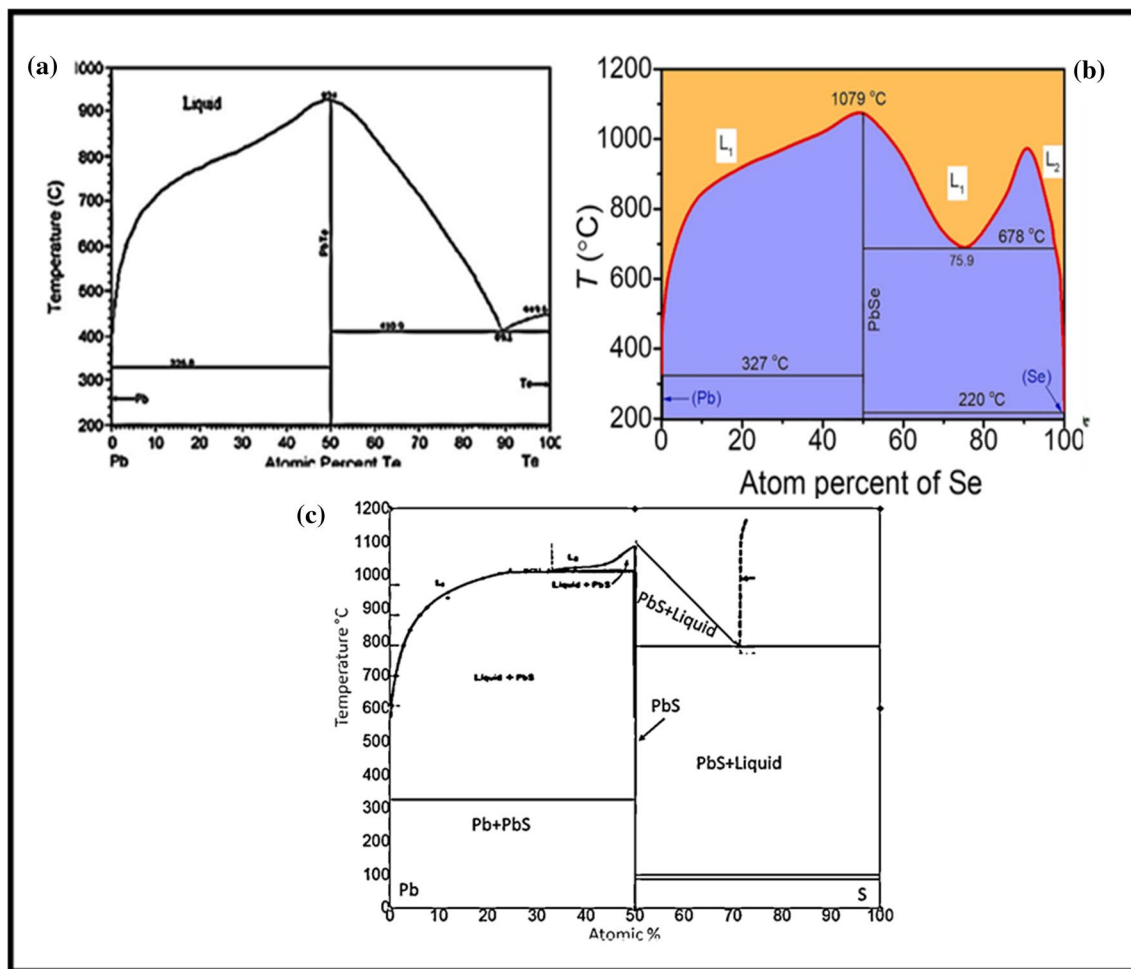
Figure 3 Binary phase diagram of **a** Pb-Te reproduced with permission [40]. Copyright 2009, Journal of Alloys and Compounds. **b** Pb-Se reproduced with permission [39]. Copyright 2022, Elsevier. **c** Pb–S [41].

In the past few decades, both theoretical and experimental researchers have paid close attention to structural phase transitions in lead chalcogenides under high pressure [46]. In normal conditions, PbTe shows rock salt structure, but it undergoes phase transition under pressure, these changes were studied on the idea of high-pressure X-ray diffraction [19, 20]. First-order structural changes in PbTe are affected by pressure. Phases in which the rock-salt structural phase modifies into an intermediary phase in the 2.2 to 6.0GPa range [48]. The PbTe compounds have shown additional structural phase transition from the intermediate phase towards the eightfold-coordinated CsCl (B2) phase at around 13 to 21 GPa. Although the intermediate phase of PbS and PbSe adopts a Tll-type of structure, it was very challenging to infer anything about the structure of PbTe from the available X-ray data, it also proposed to

belong to the GeS type. But latest X-ray diffraction studies demonstrate that the intermediate phase of PbTe and PbSe at high pressure is an orthorhombic Pnma structure observed at 6–6.7 GPa rather than the GeS or Tll type phases as initially reported [49]. The way the phonon dispersion of the NaCl phase behaves under pressure may be affected by distortions of the NaCl structure. In analyses of the dynamics of the lattice of PbTe G. Rousse et al. discovered a pressure-induced softening of PbTe. The [98] and [108] transverse acoustic phonon branch directions might be connected to the structural elements with a phase of high-pressure [18, 19].
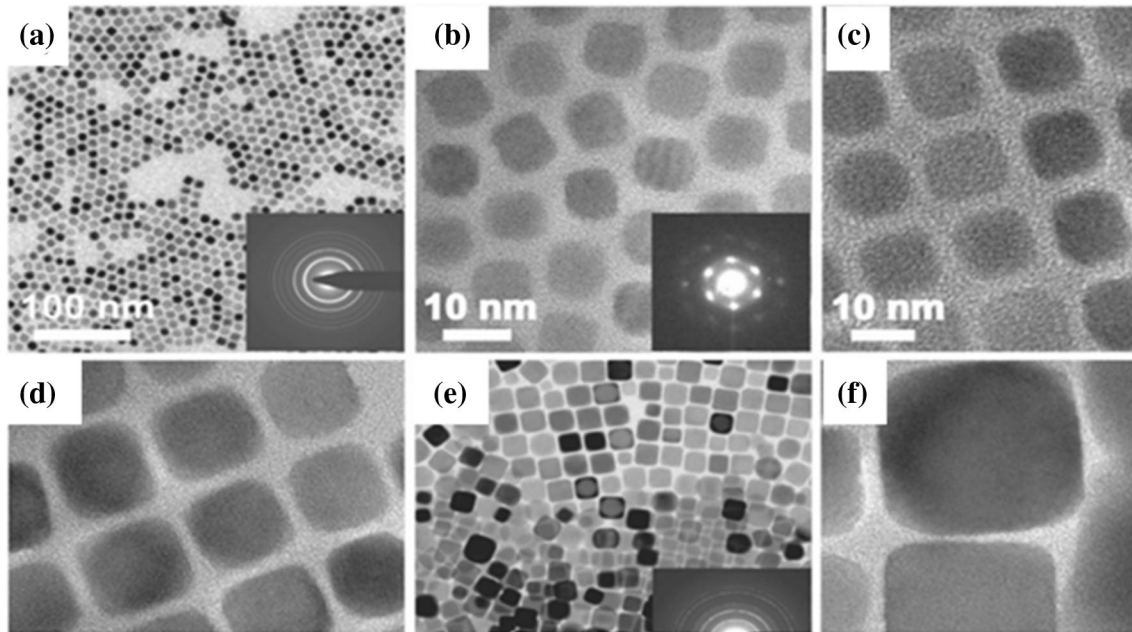
Figure 4 TEM images of **a–c** PbTe quantum dots, **d–e** PbSe quantum dots and **f** HRTEM image of PbSe, reproduced with permission [50]. Copyright 2012, Materials today.

Lead selenide (PbSe)

Figure 3b represents the Pb-Se binary phase diagram. The binary phase diagram of PbSe is a graphic depiction of the relationships that exist between the temperature, composition, and phase of a lead and selenium mixture. At various temperatures and compositions, the diagram shows the stable phases and their compositions. According to the atomic percentage composition of PbSe in the phase diagram, where Pb is 50% and Se is 50%, it indicates the stoichiometry or chemical formula of the compound. In this case, PbSe represents a 1:1 ratio of lead (Pb) atoms to selenium (Se) atoms. This means that for every lead atom, there is one selenium atom, resulting in a balanced and neutral compound. Lead selenide and Lead telluride are grouped as thermoelectric materials with a mid-temperature range. It can reach a maximum temperature of 900 K. PbSe performs better than PbTe at 900 K, melts at a relatively high temperature (1080° C), is simple to scale up, and is abundant [16]. The abundance of selenium exceeds that of tellurium by 50 times [51]. PbSe and PbTe have nearly identical electronic and structural features. The structure of PbSe, is rock salt (face-centered cubic (FCC)). In order to create the NaCl rock-salt type crystal structure with space group Fm-3 m and lattice parameter of 6.125 Å, the Pb atom is situated at the origin, while the Se atom occupies the $\left(\frac{1}{2}, \frac{1}{2}, \frac{1}{2}\right)$ position. It crystallizes as NaCl, with Pb atoms occupying the cation and Se forming the anionic lattice with extremely small energy gaps (direct gaps at the L point of 0 eV). It is a sixfold coordinated system. Figure 2c shows the structure of PbSe and Fig. 4d–f shows the TEM and HRTEM images of PbSe compound, which shows the cubic structure of the compound.

Under high pressure, there is a phase transition in PbSe [52, 53]. First-order transition is due to pressure and in normal conditions, PbSe crystallizes as NaCl under pressure and it changes to another phase. The PbSe turns to the "intermediate" orthorhombic phase at a pressure between 2.5 to 6 GPa. PbSe compounds have shown additional structural phase transitions between the intermediate phase and the eightfold-coordinated CsCl (B2) phase between 13 and 21 GPa [26, 27]. Current X-ray diffraction findings suggest that the intermediate phase of PbSe at high pressure is an orthorhombic Pnma structure observed at 6 to 6.7 GPa rather than the GeS or TlI type phases as initially disclosed [54].

Lead sulfide (PbS)

The Pb–S (lead–sulfur) binary phase diagram (Fig. 3c) depicts the relationships between temperature, composition, and the phases of a lead–sulfur mixture. At various temperatures and compositions, the diagram depicts the stable phases and their compositions. Figure 3c can be used to predict the stability of various phases of lead and sulfur mixtures. The eutectic point on the phase diagram represents the composition and temperature at which the lead sulfide compound undergoes a eutectic reaction. This reaction allows for the formation of a specific phase, often a mixture of PbS and another compound. In the case of lead sulfide, PbS is the stable phase, if the atomic percentage of Pb is 50 and S is 50, it also indicates the stoichiometry or chemical formula of the compound. PbS represents a 1:1 ratio of lead (Pb) atoms to sulfur (S) atoms. This means that for every lead atom, there is one sulfur atom, resulting in a balanced and neutral compound. The widely known group of semiconducting chalcogenides involves Lead Sulfide as one of its main elements. It is one of the most favored narrow-band-gap semiconductors with a band gap of 0.41 eV [55]. In the Earth's crust, Sulphur is one of the 16 elements with the highest abundance [51]. PbS, PbTe and PbSe have a lot in common, particularly in terms of crystal structure and energy band configuration. PbS is the lead chalcogenide that has received the least research attention due to its higher lattice thermal conductivity and consequently lower figure of merit [56, 57]. It crystallizes as a cubic crystal structure with an fm3m space group [31, 32]. The lattice parameter of PbS is defined as 5.936 Å. Pb^{2+} is bonded to six equivalent S^{2-} atoms to form a mixture of edge and corner-sharing PbS octahedral [57]. At 2.2 GPa, PbS experiences a phase transition from a NaCl-type structure to an orthorhombic structure. In normal conditions, it has a rock salt structure and, phase transition can be observed under pressure [58]. In PbX compounds, structural phase transitions were first observed by Bridgman in 1940 [59]. Later, high-pressure X-ray diffraction studies help to study the phase transition in PbS. The intermediate state is defined as Orthorhombic Pnma structure at 6–6.7 GPa. Figure 2b shows the crystal structure of PbS and Fig. 5 shows the TEM image of PbS compound which confirms the cubic structure of the compound.
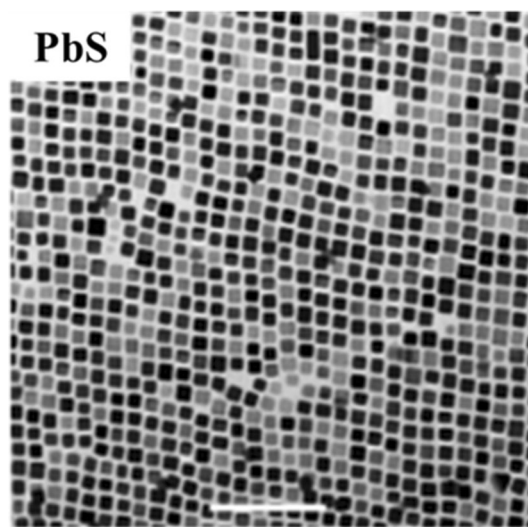

Figure 5 TEM image of PbS compound. reproduced with permission [60], Copyright 2016, Nature Communications.

Indium Chalcogenide series

Due to exceptional, controllable electrical, and thermal properties, indium chalcogenides have received significant attention in high-efficiency thermoelectrics for waste heat energy transformation [2].

Indium selenide

Figure 6a illustrates a standard In-Se binary phase diagram and demonstrates the complex stoichiometries of indium selenide, including In_4Se_3, In_2Se_3, InSe, and In_6Se [61]. Specifically, In_2Se_3 has a number of phases, such as the low-temperature phase of α'-In_2Se_3, the room temperature phases of $\alpha(2H)/(3R)$-In_2Se_3, and the high-temperature phase of $\beta(3R)$-In_2Se_3, γ-In_2Se_3, and δ-In_2Se_3 [23]. The resulting phase or phases that form can be changed by varying the atomic percentages of indium (In) and selenium (Se) within the binary system of indium selenide (InSe). The phase diagram shows the stability and composition ranges of different phases under different conditions. Here's how changing the atomic percentages affects the formation of various compounds or phases: Phase One: As previously stated, indium selenide (InSe) is formed when the atomic percentages of In and Se are in a 1:1 ratio. If the atomic percentage of either element is increased or decreased, InSe may still be the dominant phase. However, depending on the composition,
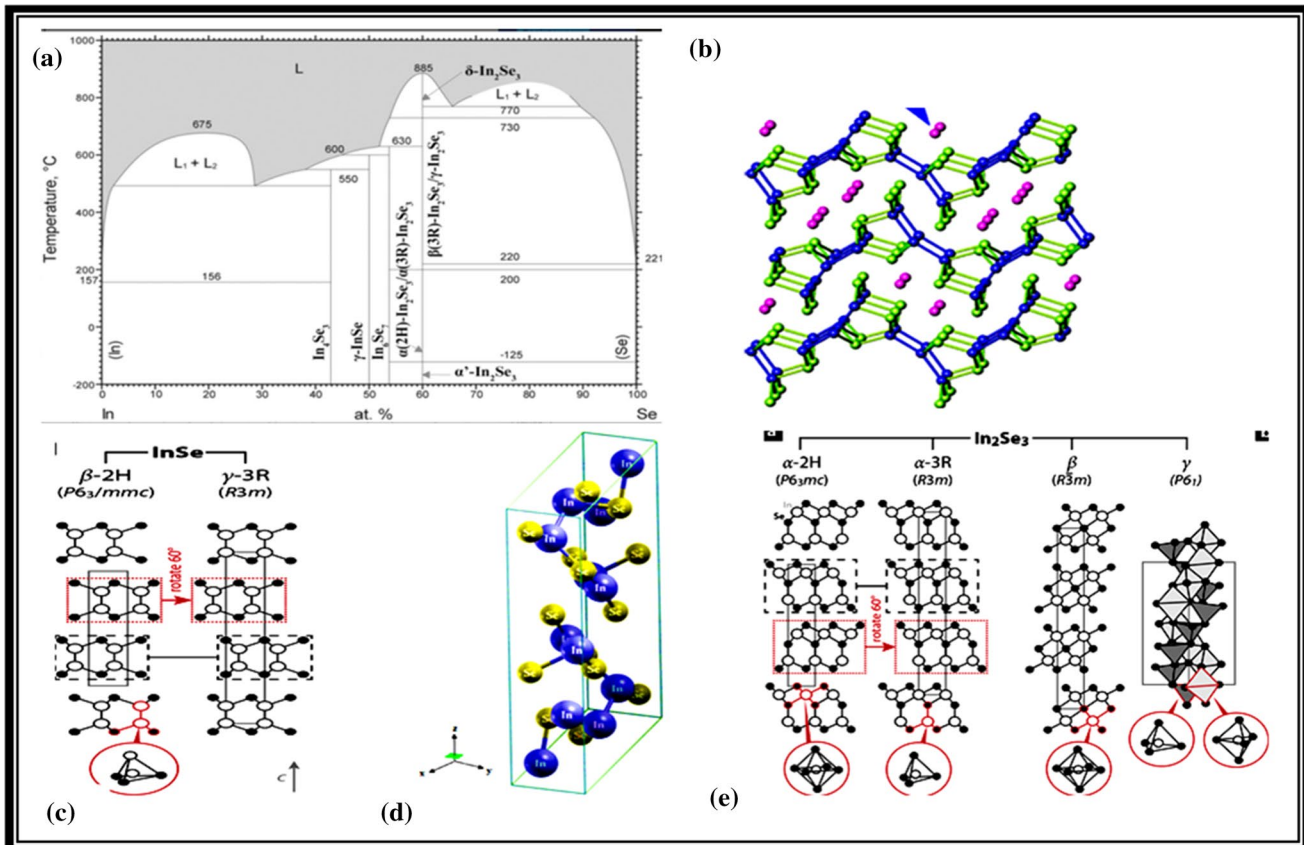
Figure 6 a Binary phase diagram of In-Se reproduced with permission [2], Copyright 2014, John Wiley and Sons. Crystal structures of **b** In$_4$Se$_3$ reproduced with permission [62], **c** InSe reported with permission [63], **d** In$_6$Se$_7$ copyright with permission [64], Copyright 2010, Physica B: Condensed Matter. **e** In$_2$Se$_3$ reported with permission [63]. Copyright 2018, ACS.

the exact boundaries and stability of InSe may change. If the atomic percentage of In is significantly greater than that of Se, you can reach a compositional range where indium-rich phases or compounds form. In$_2$Se$_3$ (indium (III) selenide) or other indium-rich selenides could be among these compounds. If the atomic percentage of Se is significantly greater than the atomic percentage of In, it may enter a compositional range where selenium-rich phases or compounds form. These compounds could contain Se or various selenides, such as In$_2$Se$_{3-X}$ (where x represents an indium deficiency). The phase diagram, once again, would provide more information on the specific composition ranges and stability of these phases.

thermal conductivity. Because of the material's complex bonding, which consists of strong covalent In-In and In-Se bonds coexisting with weaker electrostatic interactions, low thermal conductivity can be related to it. Strongly bonded $[(In_3)^{5+}(Se^{2-})_3]^-$ layers and weakly bonded In + cations are bonded together and co-exist with covalent and ionic bonds [62]. In$_4$Se$_3$'s crystal structure was identified as Orthorhombic with a Pnnm space group and respective lattice parameters are 15.297, 12.308, and 4.081 [65]. In the layered structure of In$_4$Se$_3$, as shown in Fig. 6b, the $(In_3)^{5+}$ clusters are covalently bonded to Se ions in the b-c plane, and the layers are connected along the perpendicular a-axis by van der Waals interactions. In particular, a small number of In atoms form a quasi-one-dimensional structure [66].

In$_4$Se$_3$

In$_4$Se$_3$ is an interesting n-type thermoelectric material for midrange waste heat recovery due to its low

InSe

InSe comprises of layered crystal structure with hexagonal (β-InSe) and rhombohedral (γ-InSe) faces. Rhombohedral layering (γ-InSe, R3m) organized by translation within the ab plane, and one hexagonal arranging (β-InSe, P63/mmc) with every second layer rotated by 60 degrees around [001] [63]. Hexagonal β-InSe with a space group of P6 3 /mmc and lattice parameters of $a = 4.005$ Å and $c = 16.640$ Å [67]. With a space group of R3m and lattice parameters of $a = 4.0046$ Å and $c = 24.960$ Å, γ-InSe had a rhombohedral structure [68]. The crystal structures of β-InSe and γ-InSe are shown in Fig. 6c respectively. Van der Waals interaction holds the covalently bonded layers of Se-In-In-Se in InSe together [69].

In_6Se_7

Slavnova, Luzhnaya & Medvedeva and Slavnova & Eliseev in 1963 investigated the phases present in the In-Se system and described a black crystalline phase In_6Se_7 [70]. In_6Se_7 has a monoclinic crystal structure with a P2₁ space group. The lattice parameters defined by Duffin & Hogg in 1966 are $a = 9.430$ Å, $b = 4.063$ Å, $c = 18.378$ Å with $\beta = 109.34$ Å. All other reports on In_6Se_7 are matching with the earlier reported values of Hogg [71]. Figure 6d shows the crystal structure of In_6Se_7.

In_2Se_3

In_2Se_3 shows outstanding thermoelectric properties because of the material's wide bandgap, low thermal conductivity, and high Seebeck coefficient [72]. There are various coexisting phases and crystal structures, including hexagonal/rhombohedral α/β phases in addition to hexagonal γ and δ phases are also present. The α and β phases occur in a metastable state and are subject to mutual transition when heated or cooled [73]. Since from 1910, a compound with stoichiometry In_2Se_3 has been known, and Klemm first characterized it in 1934 [74]. At ambient pressure, a minimum of four different polymorphs are present in the bulk material: α, β, γ, and δ. In addition, the 2H and 3R phases of In_2Se_3 appear to be two distinct stacking variants. Recent research has shown high-pressure phase transitions that begin from 3R In_2Se_3 [75]. In_2Se_3 crystallizes in quintuple Se-In-Se-In-Se layers. Some of these

phases, like many $A^{III}_2B^{VI}_3$ compounds, contain cation vacancies and can be categorized based on how the vacancies are arranged in the unit cell. The octet rule can only be satisfied if one-third of the cation positions are vacant, vacancies are especially common in structures where the cations only have fourfold coordination. Thus, In_2Se_3 has a layered phase without vacancies and others with vacancies [75]. α and β In_2Se_3 crystallizes in rhombohedral α/β(3R) and hexagonal α/β(2H) crystal structure. γ- In_2Se_3 crystallizes as hexagonal structure with lattice parameters $a = 7.133$ Å and $c = 19.59$ Å with space group P6₁ or P6₅. δ-In_2Se_3 crystallizes as trigonal with a space group of P3m1. The lattice parameters are reported as $a = 4.014$ Å and $c = 9.64$ Å [2]. Figure 6e shows the crystal structure of In_2Se_3 and its phases.

Indium telluride

Indium telluride shows ultra-low thermal conductivity in the mid-temperature range, and it has a band gap of approximately 1.01 to 1.13 eV [76]. Figure 7 shows the standard In-Te binary phase diagram and demonstrates the complex stoichiometries of indium tellurides, including In_9Te_7, InTe, In_3Te_4, In_2Te_3, In_3Te_5, and In_2Te_5. Specifically, In_2Te_3 and In_3Te_5 have an α and β phases. The formation of different compounds or phases in the In-Te system can be influenced by varying the atomic percentages: InTe forms when the atomic percentages of In and Te are equal. With equal atomic percentages of indium and tellurium, this composition represents the stoichiometry of InTe. A specific region on the phase diagram will indicate the stability of InTe as the dominant phase. If the atomic percentage of indium is greater than that of tellurium, the system contains an excess of indium atoms. This may result in the formation of indium-rich phases like In_2Te_3 (indium(III) telluride). On the other hand, if the tellurium atomic percentage is greater than that of indium, this indicates an excess of tellurium atoms. Tellurium-rich phases or compounds can form as a result of this. The tellurium-rich phases that form will be determined by the composition range and will be shown on the phase diagram. The presence of a phase, In_4Te_3, whose properties are identical to those of In_2Te. Additionally, the formulation In_4Te_3 agrees with the composition of 43% Te reported for the phase by Grochowski et al. [77] much better compared to the

Figure 7 Binary phase diagram of In-Te is reproduced with permission [78]. Copyright 1964, Elsevier.
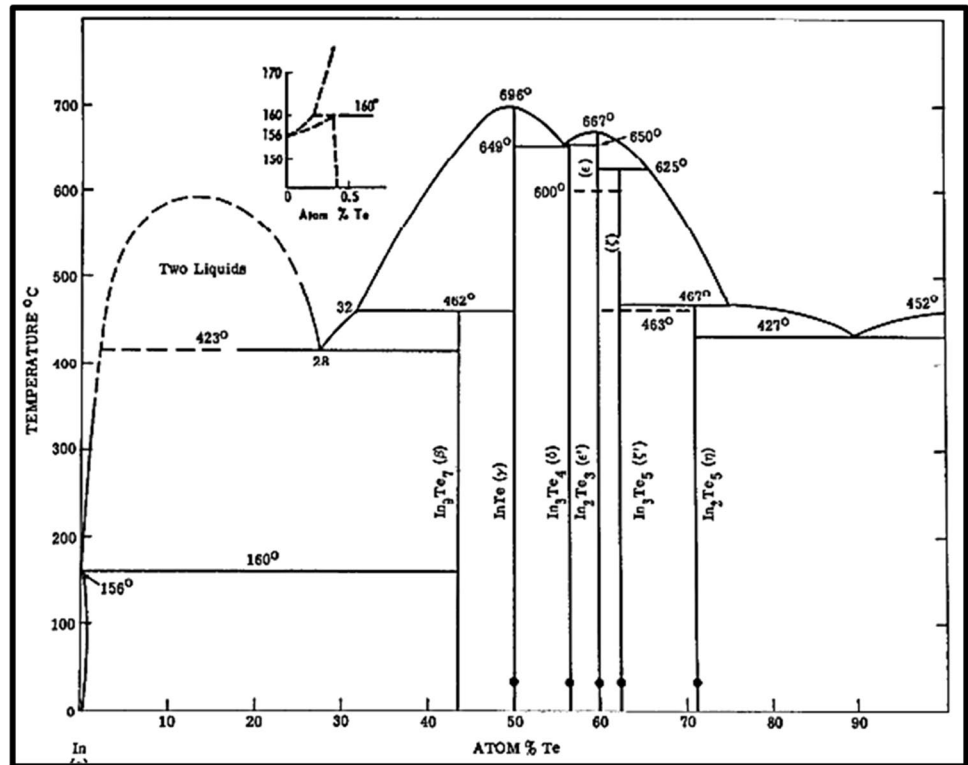
formula In_9Te_7 that they suggested. It is determined that In_2Te and In_9Te_7 should be estimated as In_4Te_3.

In₄Te₃

In_4Te_3 poses the orthorhombic Pnnm space group as the crystallization space with $a = 15.630$ Å, $b = 12.756$ Å, and $c = 4.441$ Å [76]. Figure 8a shows the crystal structure of In_4Te_3. Two different In^{1+} sites exist. In^{1+} is bonded to four Te^{2+} atoms in the first In^{1+} site in a distorted square co-planar geometry. Edge-sharing $InTe_5$ square pyramids are created in the second In^{1+} site by the bonding of In^{1+} to five Te_2 atoms. Two different In^{2+} sites exist. In^{2+} is bonded to three Te_2 atoms in the first In^{2+} site in a trigonal non-coplanar geometry. In^{2+} is bonded to three Te^{2+} atoms in a trigonal non-coplanar geometry at the second In^{2+} site. Three different Te_2 sites are present. The first Te_2 site contains a 5-coordinate geometry bond between Te_2 and two equivalents In^{2+} and three equivalents In^{1+} atoms. Te_2 is bonded in a double bond at the second Te_2 site.

InTe

InTe is a semiconducting III-VI compound that describes the $In^+In^{3+}Te$ structure. In normal conditions, InTe crystallizes as tetragonal T1Se-type (B37) with a space group of Z4/mcm and lattice parameters are $a = b = 8.63$ Å and $c = 7.23$ Å. In^+ ions are arranged by eightfold tetragonal placed anisotropic coordination by Te^{2-} ions. The two distinct crystallographic positions of the diverse chemical In^{3+} and In^+ ions inhibit the free movement of electrons from the In^+ to the In^{3+}. InTe changes to the rock salt (B1) structure with $Fm\overline{3}m$ space group and the lattice parameter $a = 6.28$ Å when hydrostatic pressures of 30 kbar and temperature in the range of 670–770 K are subjected. In this alteration, all cations are equal and are coordinated by 6 Te^{2+} ions. By removing the structural restriction on the transfer of electrons, the compound shows metallic conductivity [82]. Figure 8b shows the tetragonal and cubic structures of InTe.
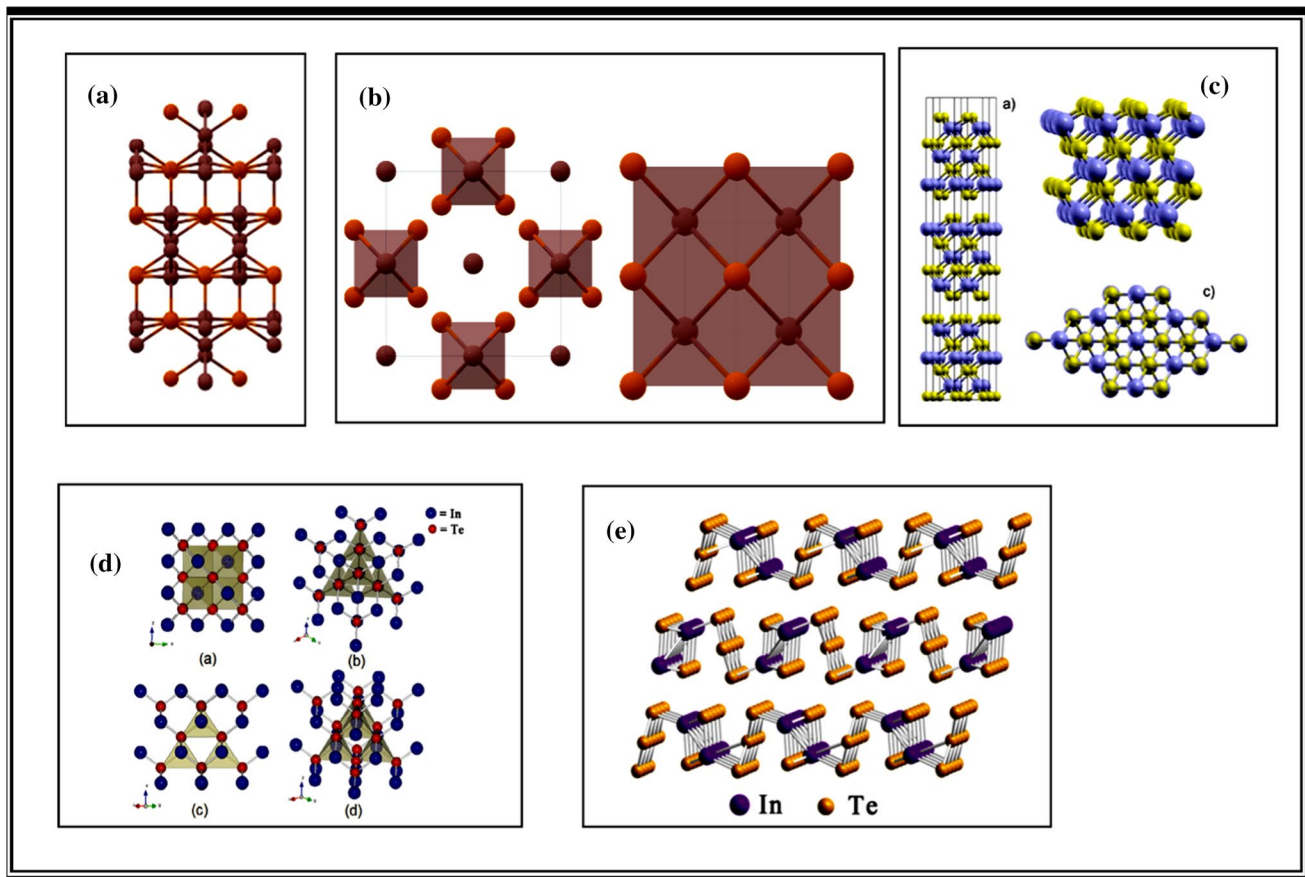
Figure 8 The Crystal structure of **a** In_4Te_3 reproduced with permission from the materials project, **b** InTe reproduced with permission from the materials project, **c** In_3Te_4 reproduced with permission [79]. Copyright 2014, John Wiley and Sons. **d** In_2Te_3 reproduced with permission [80]. Copyright 2011, Elsevier, **e** In_2Te_5 reproduced with permission [81]. Copyright 2021, Applied Physics Letters.

In_3Te_4

The bandgaps of In_4Te_3 are relatively small, measuring 0.65 eV with four atoms per unit cell, In_3Te_4 crystallizes as a layered rhombohedral structure (space group R3m). Te-In-Te-In-Te-In-Te-InTe atoms are arranged in a layer-by-layer manner and the superconductivity is observed at 1.25 K. The layers are placed together to form the 3D crystal through weak van der Waals interactions, whereas the chemical bonds within the sheets are strong and covalent, similar to other 2D materials [79]. The high thermal stability of In_3Te_4 has been demonstrated, and it can withstand heat up to 900 °C without losing any of its original properties. A rhombohedral structure with $a = 4.26$ Å and $c = 40.6$ Å was thought to exist in In_3Te_4. However, it is now known that In_3Te_4 has a tetragonal structure with $a = 6.173$ Å and $c = 12.438$ Å,

according to Karakostas et al. [83] and Fig. 8c shows the structural information of In_3Te_4.

In_3Te_5

The high-temperature form of In_3Te_5 poses a hexagonal structure, with c = 3.56 Å, a = 13.27 Å, and c/a = 0.27, as per the X-ray structure determination. There should be 16 Te-2 atoms per unit cell if all the Te-2 atoms are packed closely together in an array [78]. At T = 787 K, Grochovskii et al. predicted that the In_3Te_5 phase would form through a peritectic reaction [84].

In_2Te_3

X-ray studies have revealed that In_2Te_3 crystallizes in two polymorphic alterations, resulting in two crystal

phases of α- In$_2$Te$_3$ and β- In$_2$Te$_3$. The low-temperature α- In$_2$Te$_3$ phase belongs to the defect fluorite structure with lattice parameters of a = b = c = 6.16 Å and a = b = c = 18.54 Å, respectively. The high-temperature phase (above 523 K) is a disordered β- In$_2$Te$_3$ with a defective Zincblende structure [80]. Two modifications, denoted by α and β, respectively represent the formation at low and high temperatures. The structural framework consists of a network of distorted tetrahedral In$_2$Te$_3$ units, each of which has an In atom and three Te atoms bound to it. Neighboring units also share a Te atom [85]. Figure 8d shows the structural details of In$_2$Te$_3$.

In$_2$Te$_5$

Pentatelluride includes In$_2$Te$_5$ as a member. Klemm and Vogel have been studied this compound in 1934. It is a layered semiconducting substance with a bandgap between 0.88 and 1.26 eV [81]. Deiseroth and Amann summarized the crystal structure of In$_2$Te$_5$-I as a = 4.34 Å, b = 16.36 Å, c = 13.48 Å and In$_2$Te$_5$-II as a = 16.39 Å, b = 4.34 Å, c = 40.74 Å, respectively. According to the In-Te crystal structure data, the (In$_2$Te$_5$-I) and (In$_2$Te$_5$-II) have the monoclinic crystal system with Pearson symbols (mC28 and (mC84) and the space groups (C2/c) respectively [86]. Each layer can be described as a collection of Te chains and In-Te

chains that alternate along the a-axis. The Te chains are formed from the Te grid along the b-axis, and the In-Te chains run along it with a warped structure akin to that of NaCl. The compound's zigzag layered structure results in structural anisotropy, which helps to explain anisotropic phonon behavior. Figure 8e shows the structure of In$_2$Te$_5$.

Indium sulfide

Indium sulfide is a member of the III-VI family of semiconducting compounds. Layered crystals are some of the prominent members of this group. Like its counterparts, indium sulfide forms a tetrahedral geometry with its components. While the third S atom is unusually located in the adjacent layer, the two S atoms and one In atom are all in the same plane. Indium sulfide now has a three-dimensional network as its crystal structure. The crystal structure of indium sulfide exhibits strong anisotropy [87]. Figure 9a illustrates the standard In-S binary phase diagram and the complex stoichiometries of indium sulfide such as α-InS, β-InS, In$_6$S$_7$, and In$_2$S$_3$ have α, β and γ phases, respectively. The formation of different compounds or phases in the In-S system can be influenced by varying atomic percentages. For example, if the atomic percentage of indium is 50% and sulfur is 50%, it indicates a stoichiometric ratio in which the compound contains
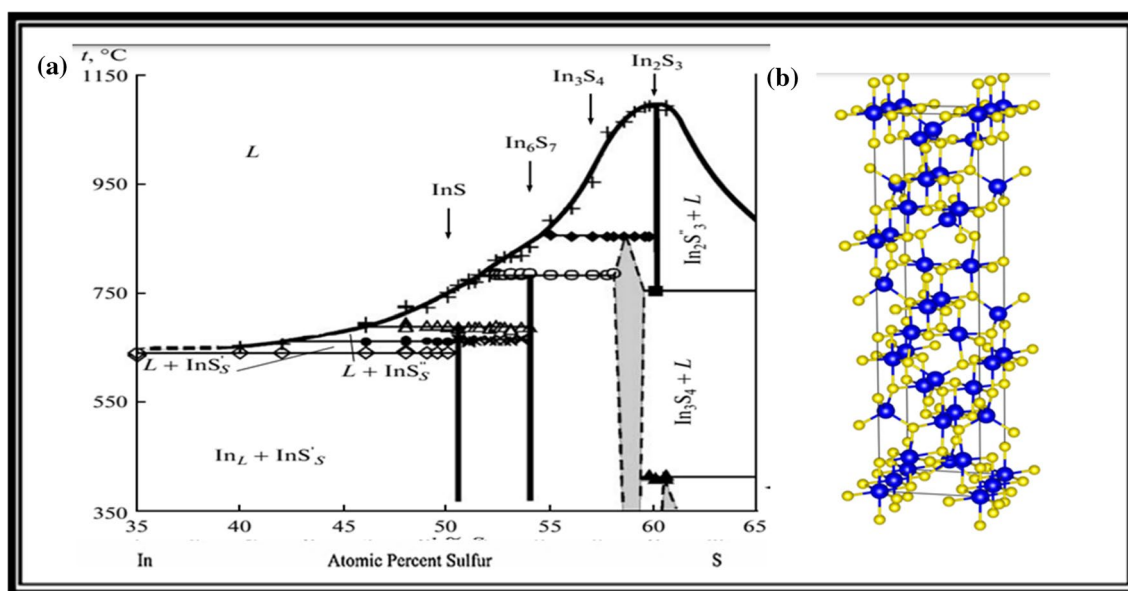

Figure 9 **a** Binary phase diagram of In-S reported with permission [88], copyright 2013, Elsevier. **b** The crystal structure of In$_2$S$_3$. Reproduced with permission [89]. Copyright 2019, American Physical Society.

an equal number of indium and sulfur atoms. InS in its purest form corresponds to this composition. If the atomic percentage of indium is greater than that of sulfur, the system has an excess of indium atoms. As a result, indium-rich phases or compounds can form. If the atomic percentage of sulfur is greater than that of indium, it indicates an excess of sulfur atoms. This can lead to the formation of sulfur-containing phases or compounds. The composition range determines the specific sulfur-rich and indium-rich phases that form, which are indicated on the phase diagram.

InS

InS crystallizes in two phases, α-InS, and β-InS as shown in the phase diagram. XRD studies confirm that InS belongs to the Hexagonal crystal system with lattice parameters $a = 3.95$ Å and $c = 10.59$ Å [23].

In$_2$S$_3$

In$_2$S$_3$ is a semiconductor with a wide band gap of around 2.4 eV. Paul Pistor et al. concluded that In$_2$S$_3$ crystallizes in α, β, and γ phases. They also reported the structures of In$_2$S$_3$. α- In$_2$S$_3$ crystallizes in a cubic crystal system with space group Fd3m. The lattice parameter a = 10.835 Å was observed at 840 K. β- In$_2$S$_3$ crystallizes in a tetragonal crystal system with a space group of 14/amd. The lattice parameters $a = 7.6231$ Å and $c = 32.358$ Å were observed at 309 K. γ- In$_2$S$_3$ crystallizes in a trigonal crystal system with a space

group of p3m1. The lattice parameters $a = 3.8656$ Å and $c = 9.1569$ Å are observed at 1099 K [90]. Figure 9b shows the crystal structure of the In$_2$S$_3$ compound.

Tin Chalcogenide series

Numerous IV-VI compounds have shown strong thermoelectric properties. Tin chalcogenides are one of these compounds, and they have excellent thermoelectric properties in the middle-temperature range (600–920 K). Tin-chalcogenides SnX (X = Te, Se, and S) have attracted research interest due to their unique qualities like low toxicity, eco-friendliness, and abundance.

Tin selenide

The two phases of tin selenide with suitable stoichiometries are shown in Fig. 10 a, such as SnSe and SnSe$_2$, which displays the standard Sn-Se binary phase diagram. Stoichiometric SnSe forms when the atomic percentages of tin and selenium are equal (i.e., when there is a 1:1 ratio). This mixture represents the ideal compound where tin and selenium are perfectly balanced atomically. An excess of tin atoms in the system is indicated if the atomic percentage of tin is higher than that of selenium. This can result in the formation of tin-rich phases, such as SnSe$_2$, where the ratio of tin to selenium is increased. The Sn-Se phase diagram illustrates the stability of different phases based on temperature and composition. SnSe is a strong thermoelectric candidate for moderate-temperature
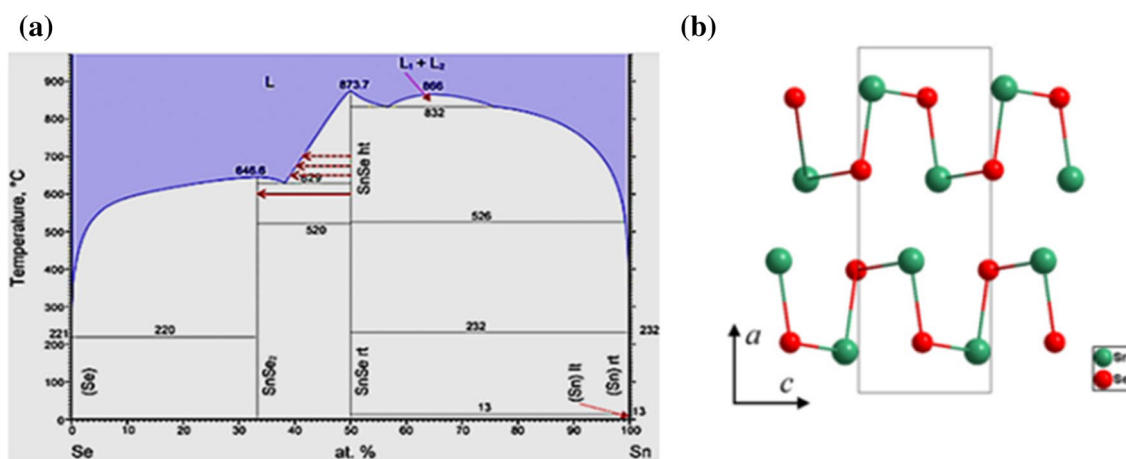

Figure 10 a Binary phase diagram of Sn-Se reproduced with permission [92], Copyright 2016, Journal of Alloys and Compounds. **b** The crystal structure of SnSe. Reported with permission [93]. Copyright 2015, Energies.

energy conversion applications. SnSe has a low thermal conductivity due to its strong anharmonicity and a high Seebeck coefficient due to its multi-valley bands [91]. SnSe/SnSe$_2$ are binary compound semiconductor materials with p/n conductivity based on tin selenide.
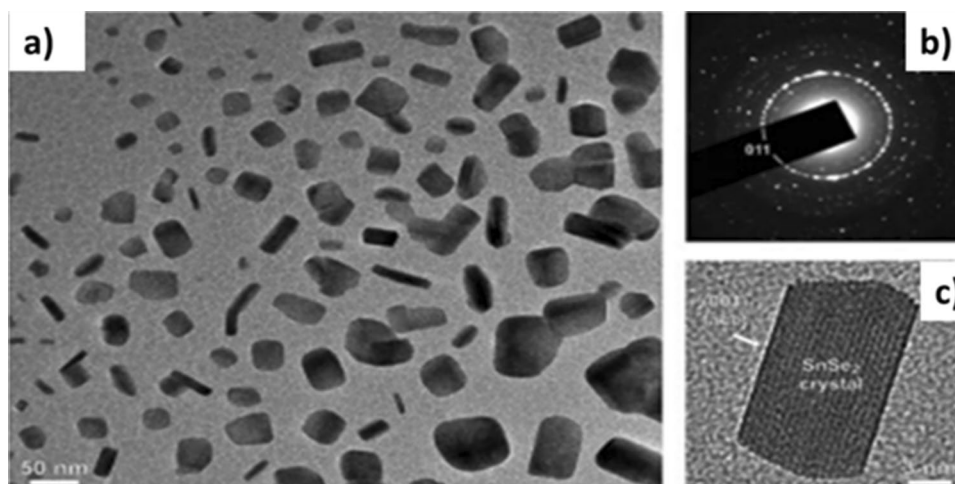
SnSe

SnSe appears in two different crystallographic phases: orthorhombic (α-SnSe) and cubic (Π-SnSe). The mechanical stability of Π-SnSe is more comparable to that of α-SnSe. Above 750 K, the orthorhombic crystal structure of SnSe showed a second-order displacive type phase transition from α-SnSe (space group Pnma) to β-SnSe (space group-Cmcm) with $a = 14.49$ Å, $b = 14.44$ Å, $c = 14.4135$ Å to $a = 14.31$ Å, $b = 14.70$ Å, $c = 14.31$ Å. The direct band gap of a-SnSe is wide and tunable, ranging from 0.98 eV (bulk) to 1.43 eV. (monolayer) [94]. Figure 10b shows the crystal structure of SnSe.

SnSe$_2$

SnSe$_2$ crystallizes in a hexagonal crystal system with a P3m1 space group, which is created by an out-of-plane van der Waals bond formation between Sn-Se-Sn slabs P3m1 (c-axis). SnSe$_2$'s lattice parameters are $a = 3.811$ Å and $c = 6.137$ Å. The band gap of SnSe$_2$ varies greatly, ranging from 1.84 eV (bulk) to 2.04 eV. (monolayer) [95]. Figure 10 b shows the structure of the tin selenide compound and Fig. 11 shows the TEM, SAED pattern and HRTEM images of SnSe$_2$ which shows the structural information of SnSe$_2$ [96].

Tin telluride

Due to similarities between their valence band structure, PbTe, and SnTe are potential to be good thermoelectric materials [97]. The conduction and valence band of SnTe at the L point of the Brillouin zone are separated by a tiny band gap (0.18 eV at 300 K), which typically produces a sizable bipolar effect. Figure 12a illustrates the Sn-Te binary phase diagram; it provides information about the stability and composition ranges of different phases of SnTe under various conditions. It shows the existence of a stable phase which is SnTe. When the atomic percentages of Sn and Te are in a 1:1 ratio, SnTe forms. This composition represents the stoichiometry of SnTe, where the atomic percentages of tin and tellurium are equal. Within the phase diagram, there will be a specific region indicating the stability of SnTe as the dominant phase.

SnTe

The lattice structure of SnTe is determined using XRD. SnTe poses cubic structure and lattice parameters are $a = b = c = 6.31$ Å and $\alpha = \beta = \gamma = 90°$ in the Fm-3 m space group [100]. In atmospheric conditions, SnTe crystallizes in a cubic structure of NaCl type. Under pressure, the phase of SnTe changes to an orthorhombic structure with pnma space group. The lattice parameters of the high-pressure phase of SnTe are $a = 11.59$ Å, $b = 4.37$ Å, and $c = 4.48$ Å. At 18 Kb pressure, the NaCl structure transforms into an orthorhombic structure [101]. Figure 12b shows the structure of SnTe and Fig. 13 shows theTEM images of precise crystal structures of SnTe compound.
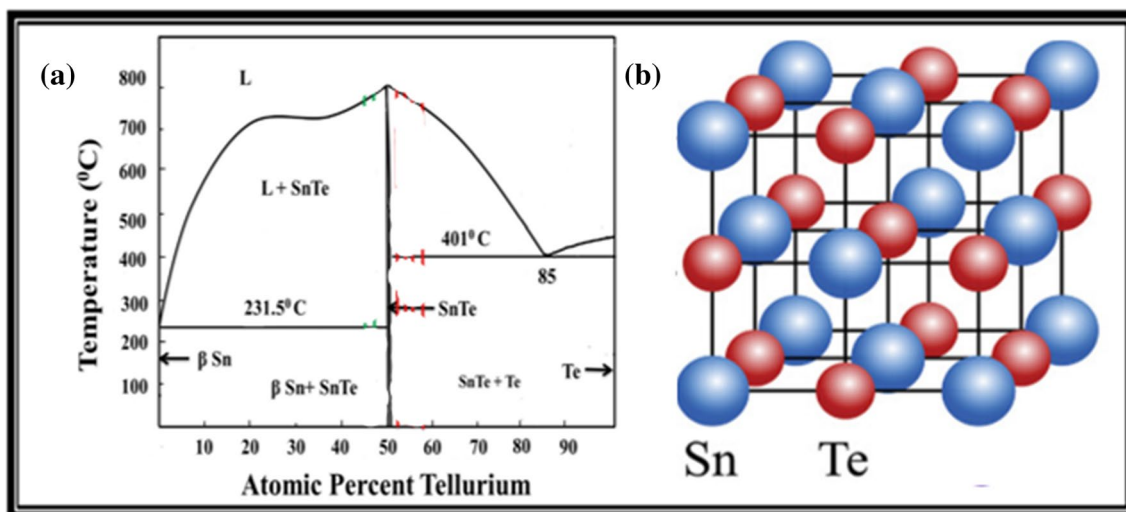
Figure 11 **a** TEM image, **b** SAED patterns, and **c** HRTEM images of SnSe$_2$ compound [96].

Figure 12 **a** Binary phase diagram of Sn-Te reproduced with permission [98], **b** crystal structure of SnTe reproduced with permission [99].
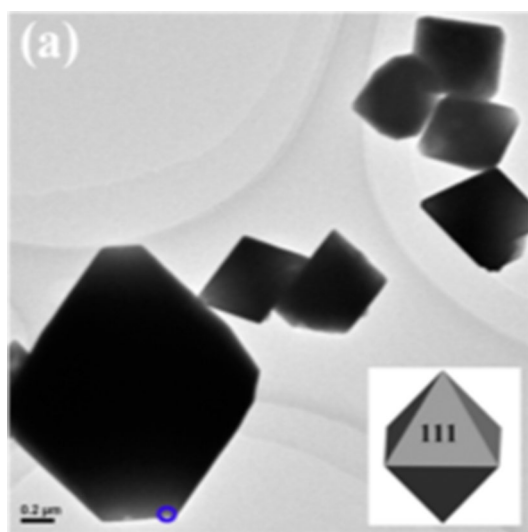

Figure 13 TEM images of SnTe compound. Reproduced with permission [102]. Copyright 2017, ACS.

Tin sulphide

A binary top group metal chalcogenide semiconductor called tin(II) sulfide (SnS) favors a layered orthorhombic crystal structure. Weak van der Waals forces that hold SnS layers together create a surface that is chemically inert, free of dangling bonds, and surface densities of states without Fermi level putting at the semiconductor surface. This gives SnS a high level of chemical and environmental reliability. As shown in the binary phase diagram in Fig. 14a. tin sulfide

has different phases like SnS, SnS_2, and Sn_2S_3 with α and β phases. In the case of tin sulfide, the phase diagram typically shows multiple phases. When the atomic percentages of Sn and S are in a 1:1 ratio, SnS forms. This composition represents the stoichiometry of SnS, where the atomic percentages of tin and sulfur are equal. Within the phase diagram, there will be a specific region indicating the stability of SnS as the dominant phase. An excess of tin atoms in the system is indicated if the atomic percentage of tin is higher than that of sulphur. This may result in the formation of phases rich in tin. On the other hand, a surplus of sulphur atoms is indicated if the sulphur atomic percentage is higher than that of tin. Sulfur-rich phases or compounds may form as a result of this. The composition range will determine the specific sulfur-rich and tin-rich phases that form, and this will be shown on the phase diagram.

SnS

Hoffman analyzed the orthorhombic crystal structure of SnS in 1935 and gave the unit cell lattice parameters of $a = 3.98$ Å, $b = 4.33$ Å, and $c = 11.18$ Å. Since the highly electronegative S atoms draw an electron pair, the structure of SnS appears to be slightly disordered in a virtual view, like that of NaCl. Additionally, the nonbonding 5 s lone pair electrons of the Sn significantly change the lattice's original rock-salt structure into a distorted orthorhombic layered structure. These disordered
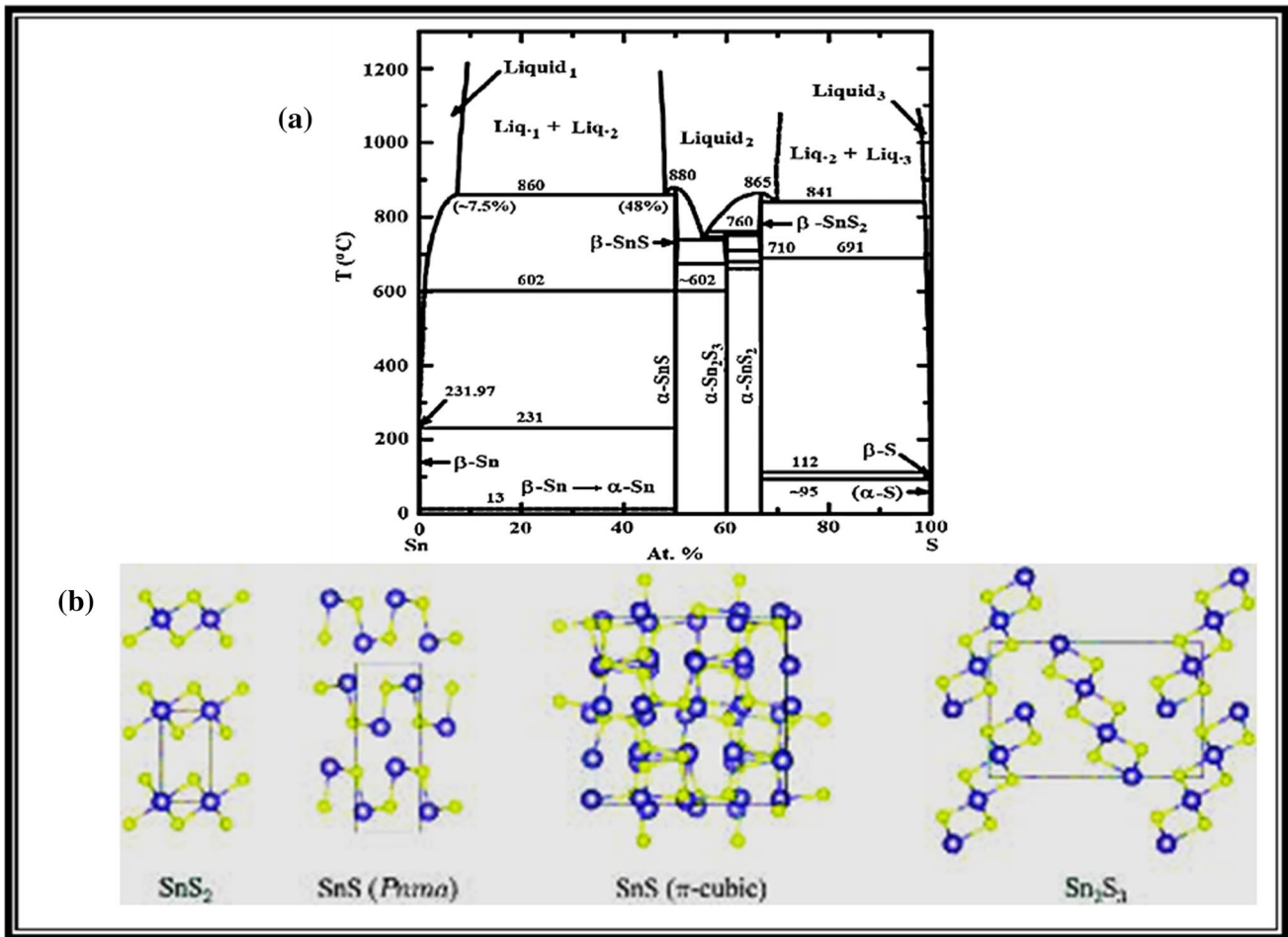
Figure 14 a Binary phase diagram of Sn-S reproduced with permission [103], copyright 2016 Elsevier **b** crystal structures of Tin Sulfide reproduced with permission [104].

layered structures have three short Sn-S bonds between each of the six "S" atoms that coordinate each "Sn" atom. The α-SnS phase of SnS is a stable low-symmetric phase. It goes through an α-type phase transition to a high-symmetric phase, or β-SnS, as the temperature rises. The orthorhombic SnS crystallographically transforms into a tetragonal one. The tetragonal phase's lattice parameters are $a = 4.23$ Å and $c = 11.51$ Å. The higher temperature phase crystallizes in a thallium iodide (TlI) type structure (B33) with the space group C_{mcm}, while the lower temperature phase crystallizes in a structure of the germanium sulfide (GeS) type (B16) with the space group P_{bnm} (D^{16}_{2h}) [105].

SnS₂

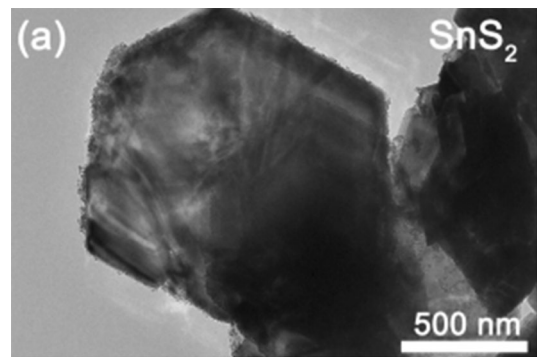SnS₂ has a hexagonal crystal system with P3m1 space group and lattice parameters of $a = 3.638$ Å and

Figure 15 TEM images of SnS₂. Reproduced with permission [107]. Copyright 2022, Elsevier.

c = 5.89 Å at room temperature. Figure 15 shows the structural information of the SnS_2. Compression in the crystal structure of SnS_2 was noticed after hydrostatic pressure of 5 GPa was applied. Pressure causes a decrease in the lattice parameters (a, c), Sn–S–Sn angle, bond lengths, and volume. Due to the layered geometry and sufficient space to compress along the c-axis, the change in lattice parameters along the c-axis is greater than the a-axis. Sn-Sn-Sn angle, interlayer distance, and bond distance are all decreasing [106].

Sn_2S_3

The equimolar mixture of SnS_2 and SnS is directly fused at a temperature of 1079 K to produce the Sn_2S_3 compound with the mixed valency of tin. Tin sequential crystallizes as an orthorhombic structure with lattice parameters of a = 8.878 Å, b = 3.751 Å, and c = 14.020 Å, whose symmetry is described by the spatial group (Pnma) [108]. Figure 14b shows the crystal structures of tin sulfide. Crystal structure and lattice parameters of some mid-temperature range chalcogenide-based TE materials are shown in Table 1.

Strategies to optimize thermoelectric performance

Bulk thermoelectric materials from the first generation, including Bi_2Te_3, PbTe, and SiGe, were created for applications at various temperatures, including room temperature, intermediate temperature, and high temperature. Controlled doping and forming solid solutions like Bi_2Te_3-Sb_2Te_3, PbTe-SnTe, and $Si_{1-X}Ge_X$ were the main strategies used in the 1960s to improve ZT value. The overall ZT enhancement is constrained because there were concurrent reductions in the charge carrier mobility, even though point defects in solid solutions serve to reduce the lattice thermal conductivity by increasing heat-carrying phonons scattering. The thermoelectric community was urged to look again at high-performance, advanced thermoelectric materials in the 1990s for uses such as cooling and thermoelectric power generation. The thermoelectric figure of merit ZT has improved in recent years, and significant progress has been made [114]. Developing and boosting the efficiency of thermoelectric samples is a tedious job because the parameters in ZT are interdependent on one another. To get high ZT, thermal conductivity should be low electrical conductivity and the Seebeck coefficient should be high. BiTe, SnSe, CuSe, half-Heusler, multicomponent oxide, organic–inorganic composite, and GeTe/PbTe series have all been found to have excellent thermoelectric properties after years of research and accumulation. Theoretically, graphene has a ZT value of 4.8 at 300 K, while Bi_2Te_3 nanowires have a ZT value of 14 when their diameter is 5 Å. Experimental measurements showed that n-type SnSe poses a ZT value of 2.8 [115]. In contrast, nanostructure engineering and defect engineering can significantly reduce thermal conductivity, bringing it closer to the amorphous limit, while manipulating the carrier concentration and band structures of materials is effective in improving electrical transport properties [116]. The best thermoelectric materials, according to conventional wisdom, combine an electronic crystal structure with an amorphous phonon glass to produce a glass-like lattice with low thermal conductivity. The carrier mobility in the electron crystal region is unaffected by hosting disorders in the phonon glass region or by doping to block phonons [3]. To optimize the parameters and to achieve a high-power factor, low thermal conductivity, or a combination of the two, a number of strategies have been used. By using the right carrier doping, quantum confinement, energy carrier filtering, reducing the effective mass, and alloying the band structure, the power factor can be improved [117]. Interfaces could be added to materials to reduce thermal conductivity and to increase phonon scattering at the atomic, nanoscale, and microscale through alloying, nanostructuring, or multiscale hierarchical engineering [118]. This review emphasized the crucial techniques for improving mid-temperature thermoelectric material's thermoelectric performance, which will motivate researchers to investigate more about these thermoelectric materials. It is important to note that the improvement of thermoelectric properties is not constrained to the application of a single technique. In several studies, multiple techniques have been used concurrently to achieve the greatest improved performance in thermoelectric results. The creation of high-performance thermoelectric materials and the associated thermoelectric theory are therefore seeing increasing interest. Two distinct strategies have been developed over the past twenty years to find the next generation of thermoelectric

Table 1 Crystal structure and lattice parameters of some mid-temperature range chalcogenide-based TE materials

Sl no.	Material	Crystal structure	Lattice parameters	Refs.
1	PbTe	NaCl (rock salt), Fm3m	a = 6.460 Å	[43]
2	PbSe	NaCl (rock salt), Fm $\overline{3}$ m	a = 6.125 Å	[51]
3	PbS	NaCl (rock salt), Fm $\overline{3}$ m	a = 5.930 Å	[51]
4	PbTe	NaCl (rock salt), Fm3m	a = 6.448 Å	[35]
5	PbSe	NaCl (rock salt), Fm3m	a = 6.104 Å	[35]
6	PbS	NaCl (rock salt), Fm3m	a = 5.905 Å	[35]
7	PbTe	Orthorhombic Pnma,(at 6.7GPa)	a = 8.157 Å, b = 4.492 Å, and c = 6.294 Å	[47]
8	$Pb_{1-X}Sn_XSe$	NaCl, Fm3m	a = 6.0337 Å	[54]
9	$Pb_{1-X}Sn_XTe$	NaCl (rock salt), Fm3m	a = 6.3505 Å	[54]
10	PbS	Face-centered cubic, Fm3m	a = 5.9362 Å	[41]
11	In_2Te_5	Monoclinic, C2/c	a = 16.66 Å, b = 4.36 Å, and c = 41 Å	[81]
12	In_3Te_4	Rhombohedral, R $\overline{3}$ m	a = 4.26 Å, c = 40.6 Å	[109]
13	In_3Te_4	Tetragonal	a = 6.173 Å, c = 12.438 Å	[109]
14	In_3Te_5	Hexagonal	a = 13.27 Å, c = 3.56 Å	[78]
15	In_4Te_3	Orthorhombic, Pnnm	a = 15.630 Å, b = 12.756 Å, c = 4.441 Å	[76]
16	α(2H)-In_2Se_3	Hexagonal, $P6_3$/mmc	a = 4.025 Å, c = 19.235 Å	[61]
17	α(3R)-In_2Se_3	Rhombohedral, R3m	a = 4.05 Å, c = 28.77 Å	[110]
18	β(2H)-In_2Se_3	Hexagonal, $P6_3$/mmc	a = 4.0157 Å, c = 19.222 Å	[111]
19	β(3R)-In_2Se_3	Rhombohedral, R $\overline{3}$ m	a = 4.000 Å, c = 28.33 Å	[61]
20	γ-In_2Se_3	Hexagonal, $P6_1$	a = 7.1286 Å,c = 19.381 Å	[111]
21	δ-In_2Se_3	Trigonal, P3m1	a = 4.0181 Å, c = 9.646 Å	[61]
22	In_3Se_4	Rhombohedral, R $\overline{3}$ m	a = 3.964 Å, c = 39.59 Å	[83]
23	β-InSe	Hexagonal, $P6_3$/mmc	a = 4.005 Å, c = 16.64 Å	[61]
24	γ-InSe	Rhombohedral, R3m	a = 4.002 Å, c = 24.946 Å	[68]
25	In_4Se_3	Orthorhombic, Pnnm	a = 15.30 Å, b = 12.18 Å, c = 4.050 Å	[112]
26	In_6Se_7	Monoclinic, $P2_1$/m	a = 9.433 Å, b = 4.064 Å, c = 17.663 Å, β = 100.92°	[113]
27	InTe	Tetragonal T1Se-type (B37), Z4/mcm	a = b = 8.63 Å, c = 7.23 Å	[82]
28	β-In_2Te_3	Cubic, F $\overline{4}$ 3 m	a = 6.158 Å	[85]
29	α-In_2S_3	Cubic, Fd3m	a = 10.835 Å	[90]
30	β- In_2S_3	Tetragonal, 14/amd	a = 7.6231 Å, c = 32.358 Å	[90]
31	γ- In_2S_3	Trigonal, p3m1	a = 3.8656 Å, c = 9.1569 Å	[90]
32	α-SnSe	Orthorhombic, Pnma	a = 14.49 Å, b = 14.44 Å, c = 14.4135 Å	[94]
33	β-SnSe	Orthorhombic,Cmcm	a = 14.31 Å, b = 14.70 Å, c = 14.31 Å	[94]
34	$SnSe_2$	Hexagonal, P3m1	a = 3.811 Å, c = 6.137 Å	[95]
35	SnTe	Cubic, Fm3m	a = 6.31 Å	[100]
36	α-SnS	Orthorhombic, Cmcm	a = 3.98 Å, b = 4.33 Å, c = 11.18 Å	[105]
37	β-SnS	Tetragonal	a = 4.23 Å, c = 11.51 Å	[105]
38	SnS_2	Hexagonal, P3m1	a = 3.638 Å, c = 5.89 Å	[106]
39	Sn_2S_3	Orthorhombic, Pnma	a = 8.878 Å, b = 3.751 Å, c = 14.020 Å	[108]

materials. The first is the discovery and application of novel families of bulk thermoelectric materials with intricate crystal structures, and the second is the synthesis and application of low-dimensional thermoelectric material systems [114]. Thermoelectric performance can be enhanced through doping, nanostructuring, nanocomposite, alloying, and co-doping [3]. The following flowchart (Fig. 16) can give some idea of how to increase thermoelectric

Figure 16 Flowchart to optimize the thermoelectric performance
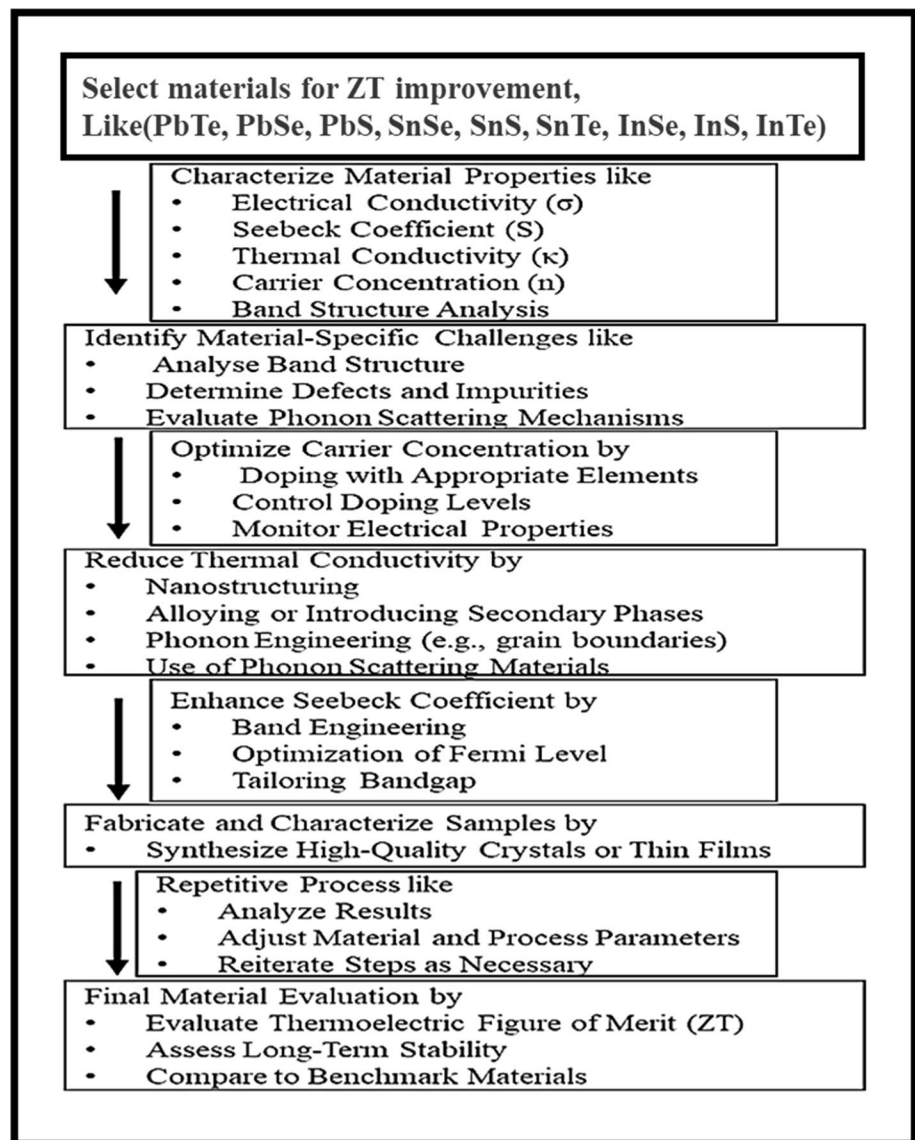
efficiency and some of the strategies are explained in detail in the below of the flowchart (Figs. 17, 18).

Doping

Doping helps to manage the carrier concentration to get high efficiency in the TE materials and also helps to reduce thermal conductivity by generating scattering centers for phonons and to generate defects. By increasing dopants, the density of states can be increased this helps to monitor Seebeck co-efficient and also increases electrical conductivity. Parker and Singh studied the doping of PbSe and they reported that the heavily doped PbSe sample gives ZT ~ 2 in the mid-temperature range [119]. Heng Weng

et al. reported that Na-doped PbSe gives ZT ~ 1.2 at 850 K, and Na provides a high hole concentration in the system [120]. Sn, I, and Ti-doped PbTe showed enhanced ZT of about 50% compared to pristine and ZT reaches up to 1.5 at 773 K [37]. Yihuai Li et al. reported that Bi-doped PbS shows ZT up to 0.89 at 773 K, excellent electrical conductivity due to the use of Bi^{3+} doping to modify carrier concentration and mobility and declined thermal conductivity through the use of the right defect [17]. Recently, SnSe, a layered chalcogenide material, has received a lot of attention for its amazing p-type thermoelectric property, notable ZT value of 2.6 at 923 K. At 733 K, the n-type SnSe single crystal has a maximum ZT value of 2.2 along the b axis shown in Fig. 19 and corresponding
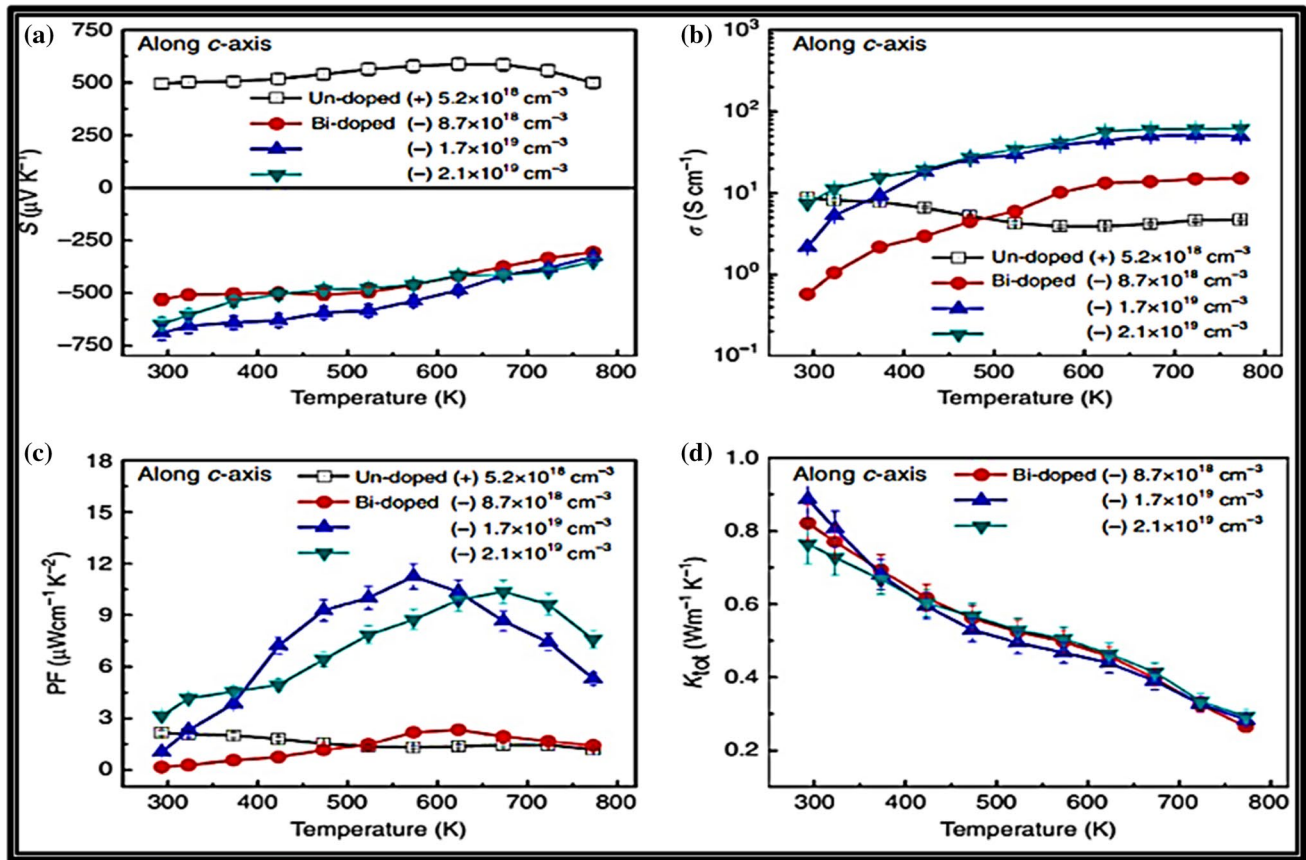
Figure 17 Thermoelectric properties of undoped and Bi-doped SnSe along different c-axis **a** S **b** σ **c** PF **d** κ_{to} Reproduced with permission [118].

ZT along a,c axis shown in Fig. 19a and a carrier density of $2.1 \times 10^{19} Cm^{-3}$. Figure 17 a displays the temperature-dependent Seebeck coefficient for undoped and bi-doped SnSe single crystals across the c-axis. All Bi-doped samples have n-type nature, with a Seebeck coefficient ranging from 520 to 730 mV K^{-1} at 300 K, whereas the undoped sample exhibits p-type nature and has a Seebeck coefficient of 500 mV K^{-1} at 300 K. The value of Seebeck coefficient of Bi-doped SnSe single crystals reduces with temperature, whereas it raises with temperature for undoped SnSe until 650 K. Figure 18b displays the temperature-dependent electrical conductivity of SnSe and Bi-doped SnSe along the c axis. Electrical conductivity for all the n-type samples raises from room temperature to high temperatures, whereas it reduces in the undoped sample below 600 K. High electrical conductivity in n-type SnSe is caused by an increase in electron carrier concentration brought on by Bi doping. Figure 17c depicts the temperature-dependent power factor (PF). Due to the low electrical conductivity, small PF values have

been observed in p-type SnSe and in lightly Bi-doped samples. The highest PF values observed in highly Bi-doped SnSe are 10.36 and 11.25 mW cm^{-1} K^{-2} at 673 and 573 K, respectively. As demonstrated in Fig. 17d, the total thermal conductivity of Bi-doped SnSe single crystals has been measured over the temperature range of 300 to 773 K. The findings indicate that the κ_{tot} values for the three distinct Bi-doped contents have been comparable. It has been noted that the lattice phonons dominantly contribute to κ_{tot} in semiconductors. Therefore, the effect of electron carriers in κ_{tot} within n-type samples is minimal. The noted thermal conductivities of p-type SnSe, 0.23, 0.33, and 0.3 Wm^{-1} K^{-1}, along the a, b, and c axes shown in Fig. 18c at about 773 K, are comparable to the thermal conductivity values of n-type SnSe single crystals and corresponding Seebeck coefficient, thermal conductivity and electrical conductivity are shown in Fig. 17d, 18a, b [118]. Qian Zhang et al. showed that at around 873 K, 0.25 atom% In-doped SnTe showed a maximum ZT value of 1.1 and they explained that
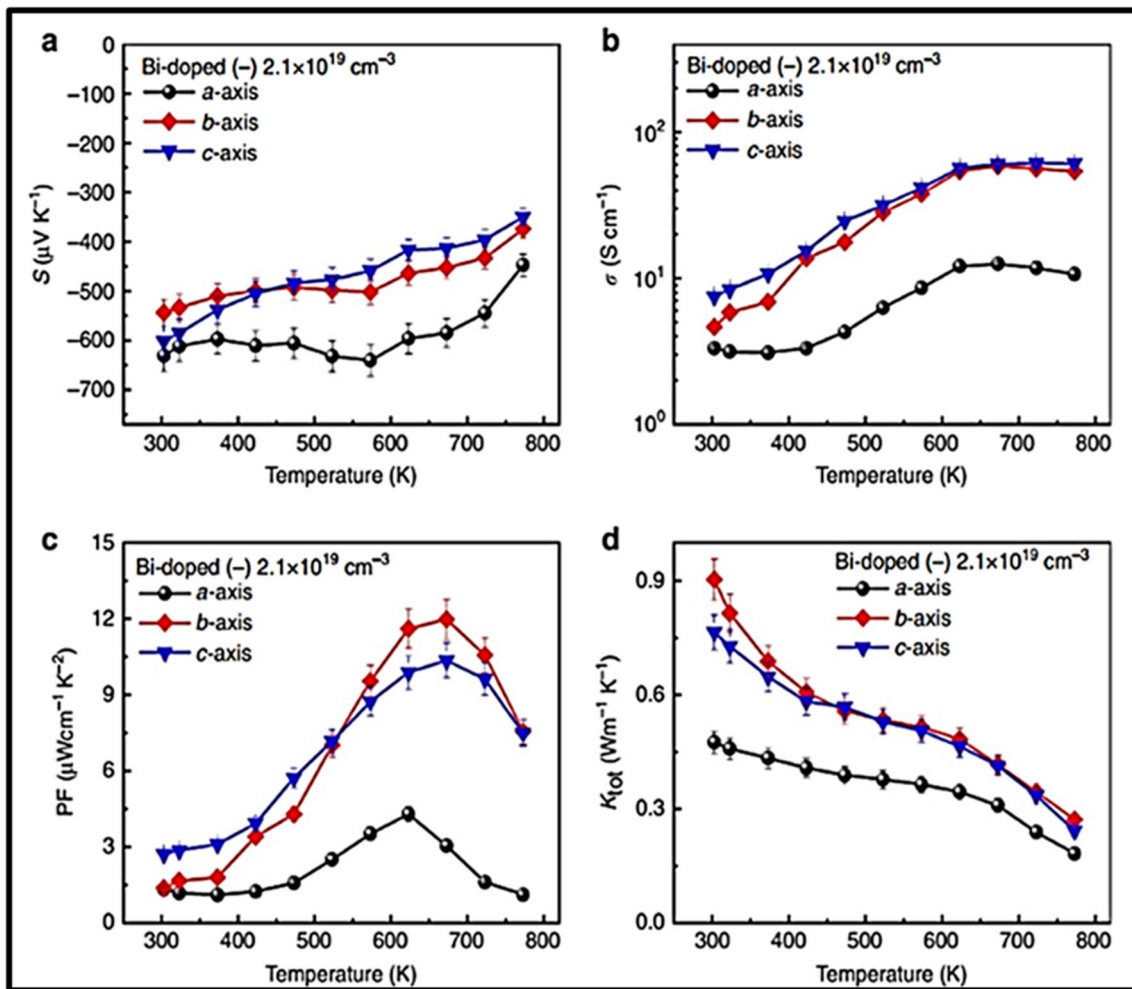
Figure 18 Thermoelectric properties o Bi-doped SnSe along different axis **a** S **b** σ **c** PF **d** κ_{tot} Reproduced with permission [118].
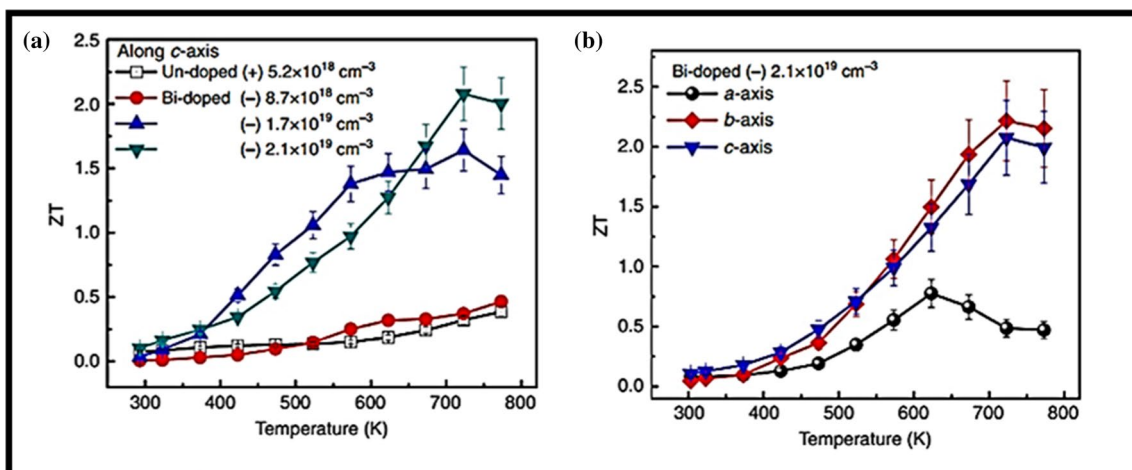

Figure 19 **a** ZT of undoped and Bi-doped SnSe along c-axis, **b** ZT of Bi-doped SnSe along different axis. Reproduced with permission [118].
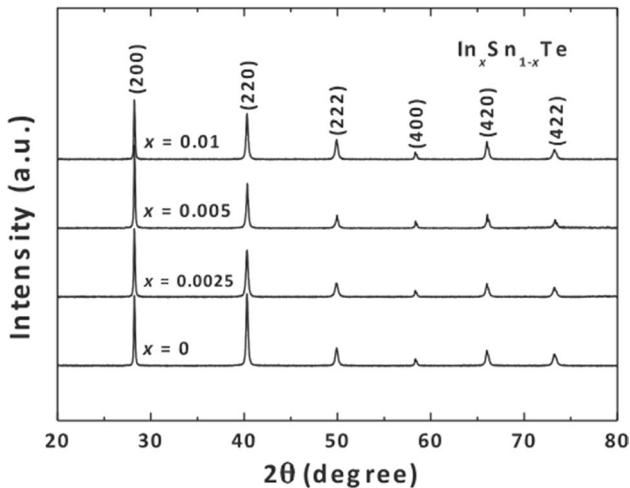
Figure 20 XRD patterns for the $In_xSn_{1-x}Te$ ($x=0$, 0.0025, 0.005, and 0.01) material [121].

the In substitutes Sn in SnTe compound and it can be confirmed by the XRD pattern shown in Fig. 20 [123]. Binqiang Zhou et al. reported the Na-doped SnS sample with a maximum ZT value of 0.8 at 850 K increased carrier concentration by nearly about $\sim 1 \times 10^{20}$ cm^{-3} [122]. According to Jong-Soo Rhyee et al. ZT has been significantly increased, reaching a maximum value of 1.53 over a wide temperature range in chlorine-doped materials. In the $In_4Se_{3-x}Cl_{0.03}$ compounds, the electrical conductivity primarily increases due to a rise in both carrier concentration and Hall mobility, and high thermoelectric output was found to exist due to charge density wave lattice instability along crystallographic bc plane. As temperature rises, the main cause for the decrease in thermal conductivity is the contribution of acoustic phonons [123]. The large electronic affinity of Cu compared to Na was shown by Huaxing Zhu et al. and are able to effectively reduce the Coulomb scattering for charge carriers. As a result, at 730 K, the maximum figure of merit ZT for InTe is found to be approximately 0.73 [124].

Co-doping

Recently co-doping has experienced extensive research and is a promising method for enhancing the performance of thermoelectric materials. Co-doping is a strategy where different dopants are added to the cationic and anionic sides of the base compound to improve their efficiency. The dopant's selection is mainly based on the atomic radius of the

base element. If the atomic radius of the dopant is greater than the matrix element the crystallite size increases, on the other hand, if the atomic radius of the dopant element is smaller compared to the matrix element, then the crystallite size decreases. By lowering the ionization energies of acceptors and donors, co-doping can effectively increase the dopant solubility, activation rate, and carrier mobility [125]. This technique of co-doping two resonant dopants not just to improves the material's efficiency across the temperature range, but also inspires researchers to seek out other, unusual combinations of dopants to fruitfully optimize the material's electronic structure [126]. Haotian Fan et al. explained the effect of co-dopants like Ag-Sb to the PbSe and how thermal conductivity is reduced based on HRTEM images. An HRTEM image of the Ag-Sb co-doped PbSe sample in Fig. 21c demonstrates the presence of features at the nanoscale. It is evident that the crystal grains contain a number of well-crystallized nano-regions and wavy patterns that are several nanometers wide. These PbSe nanostructures with Ag and Sb doping would effectively scatter phonons to reduce the thermal conductivity of the lattice. Additionally, micrograins contain a lot of dislocations (Fig. 21c(2) and c(3)). These flaws cause the lattices to be severely twisted and distorted, which would strongly scatter phonons. These flaws should result from nanoscale elemental fluctuations [127]. Sandhya Shenoy et.al studied the tailoring of SnTe's electronic structure through the co-doping of Zn with Ag, Ca, and Mg and they explained how the dopants enhance the thermoelectric performance and play complementary roles. While M (M = Ag, Ca, Mg) widens the band gap, thus preventing bipolar transportation and aids in improving the band convergence performance at higher temperatures. The band gap widening enhances thermoelectric performance by decreasing bipolar transport, minority carriers' ability to contribute to Seebeck, and carriers' ability to conduct heat across the band gap. When Zn is codoped, resonance states develop as a doubly degenerate split-off band from the initially eight-fold degenerate valence band maxima. Zn introduces resonance level and causes hyper-convergence to increase the Seebeck at low temperatures. Additionally, they simulated electronic structure of co-doped SnTe samples to examine the co-doping's effects (Fig. 21a). Compared to $Sn_{14}AgZnTe_{16}$, the band gap of $Sn_{16}Te_{16}$ is found to increase from 0.081 eV to 0.329 eV. Zn further modifies the electronic structure, and this property is known
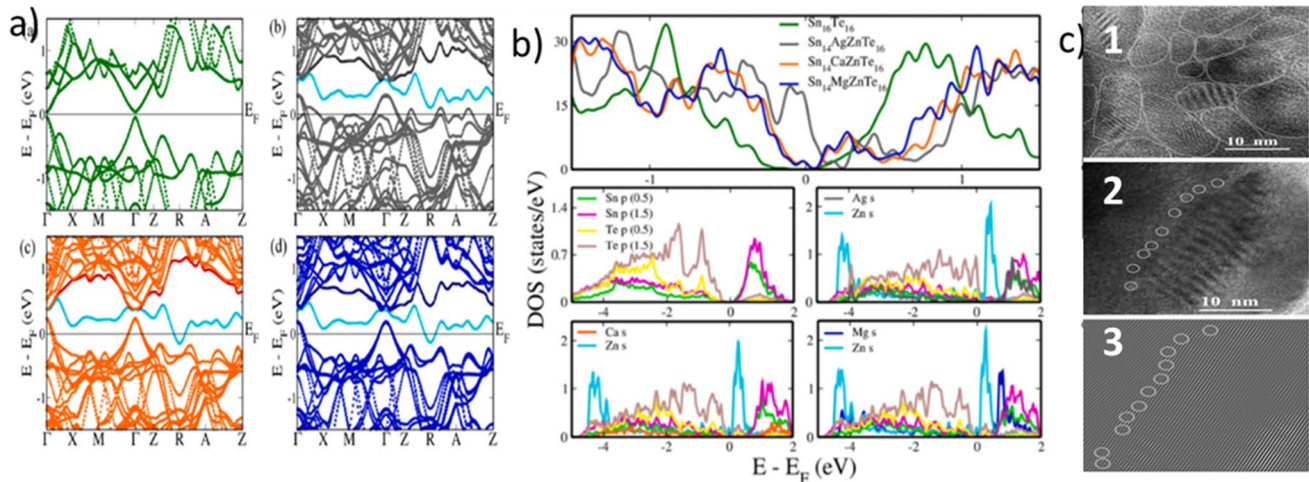
Figure 21 a Electronic structure and **b** DOS of SnTe and co-doped SnTe, Reproduced with permission [128]. Copyright 2021, Elsevier **c** HRTEM image of Ag-Sb doped PbSe, C.1) showing grain boundaries and dislocations (C.2) and (C.3) detailed view of dislocations in C.2. Reproduced with permission [127]. Copyright 2015, Elsevier.

to raise the Seebeck values at room temperature by increasing the proportion of degenerate valley that contribute to the transport properties. The change in the conduction band region caused by the addition of M (M = Ag, Ca, Mg) is an intriguing aspect worth mentioning in this context. A heavy electron conduction band is generated at the R point as a result of the loss of the degeneracy of the conduction band minima. The light electron conduction band is converged as the dopant is switched from Ca (0.723 eV) to Ag (0.191 eV) to Mg (0.012 eV). This shows that the dopant can successfully alter the conditions to act as an n-type and also enhance the transport properties in an n-type material. In contrast to pristine SnTe, co-doped samples showed prominent peaks closer to the Fermi level in their densities of states (DOS) (Fig. 21b). The partial density of states (pDOS) plot demonstrates that in SnTe, Te 'p' orbitals form the valence states and Sn 'p' orbitals as conduction states. They noticed that as the temperature rose, the electrical conductivity values decreased, indicating the semiconductor's typical degenerate nature [124]. Some of the mid-temperature materials doped and co-doped with different elements and their thermoelectric figure of merit, ZT are listed in Table 2 (Fig. 22).

Alloying

Alloying of elements was found to be a successful strategy for enhancing ZT but in a different way than the doping effect. The process of combining two or more metallic elements to form an alloy is known as alloying. An alloy is a substance made of different metals or metals combined with one or more non-metallic elements. In order to meet particular requirements for various applications, alloying is used to improve specific properties of the base metal(s). The ability of alloy formation to scatter heat-carrying phonons and improve the performance of thermoelectric materials has also been widely recognized since the 1950s. By using alloy scattering, it is possible to significantly improve both the electronic properties and the lattice thermal conductivity [149]. In order to understand their impacts on lattice strains for k_L-reduction, it also controls the defect structures involving both dense in-grain dislocations and precipitate-induced interfaces at low temperatures and they reported the reduced thermal value as 0.8 W m^{-1} K^{-1} as shown in Fig. 23c. In NaYEu$_{0.03}$Cd$_{0.03}$Pb$_{0.9-y}$ the maximum Seebeck co-efficient (310 µv/K) is reported for Y = 0.010 concentration at 850 K as shown in Fig. 23a and maximum resistivity is about 6.3mΩcm for Y = 0.010 concentration as shown in Fig. 23b. The maximum ZT of about 2.5 for Y = 0.030 concentration at 850 K as shown in Fig. 23d [150]. Tian-Ran Wei et al. combined PbSe and p-type polycrystalline SnSe, they reported that due to strain and mass fluctuations, the lattice thermal conductivity decreased by 12 at.% from 1.4 to 0.85 W m^{-1} K^{-1}. It's interesting to note that the Pb substitution has little effect on the Seebeck coefficient and carrier concentration,

Table 2 List of some mid-temperature materials doped and co-doped with different elements and their thermoelectric figure of merit, ZT

Sl.No	Material	Type	Method	Dopant	ZT	T (K)	Ref
1	PbTe	*p*	MG	Na	1.3	700	[129]
2	PbTe	*p*	BM+HP	Tl	1.3	673	[130]
3	PbTe	*n*	M+Q+BM	Bi	1.1	773	[15]
4	PbSe	*n*	BM+HP	Al	1.3	850	[131]
5	PbSe	*n*	MG	Ga	0.9	900	[132]
6	PbSe	*n*	MG	In	0.8	700	[132]
7	PbS	*n*	A+G+HP	Cl	0.7	850	[56]
8	PbS	*n*	HT	Bi	0.89	773	[17]
9	SnSe	*p*	M+HP	Zn	0.96	873	[133]
10	SnSe$_{1-X}$S$_X$	*n*	M+HP	I	0.8	773	[134]
11	SnSe	*n*	GGM	Bi	2.2	773	[118]
12	SnSe	*n*	M+BM+HP	Br	1.3	773	[135]
13	SnSe	*p*	HT	Cu	1.2	873	[136]
14	SnTe	*p*	BM+HP	In	1.1	873	[121]
15	SnTe	*p*	M+SPS	SrTe	1.2	823	[137]
16	SnTe	*p*	M+SPS	Bi	0.9	823	[137]
17	SnTe	*p*	MG	Mg	1.2	860	[97]
18	SnS	*p*	Bm	Na	1.1	870	[138]
19	SnS	*p*	MA+SPS	Ag	0.6	873	[139]
20	SnS	*p*	M+Q+A	Na	0.65	800	[122]
21	In$_2$Se$_3$	–	M+BM+SPS	Cu	0.55	846	[72]
22	In$_4$Se$_3$	*n*	Bm	Cl	1.53	698	[123]
23	InSe	–	DFT	Bi	0.65	800	[140]
24	In$_4$Te$_3$	*n*	SPS	Se	0.56	670	[22]
25	InSe	*n*	SPS	Sn	0.66	700	[21]
26	In$_4$Se$_3$	*n*	Bm	Cu	0.97	723	[141]
Co-doping							
27	PbTe	*n*	MG	Cr and I	2.0	500	[142]
28	PbSe	*p*	High-pressure	Ag and Sb	1.03	600	[127]
29	PbTe	*p*	MG	K and Na	1.3	700	[143]
30	SnSe	*n*	MA+SPS	Ti and Pb	0.4	773	[144]
31	SnSe	*n*	M+SPS	Na andAg	1.2	785	[145]
32	SnTe	*p*	HP	Bi and Zn	1.6	840	[126]
33	SnTe	*p*	M+Q+HP	In and Se	0.9	873	[146]
34	SnTe	*p*	M+Q+HP	Ge,Sb and Bi	1.1	873	[147]
35	In$_4$Se$_3$	*n*	SSR+SPS	Pb and Sn	1.4	733	[148]

The abbreviations listed in the column for the synthetic technique stand for the following ideas: *BM* ball milling, *HP* hot pressing, *M* melting, *MG* melt growth, *Q* quenching, *A* annealing, *G* grinding, *HT* hydrothermal method, *GGM* Gradient growth method, *SPS* spark plasma sintering, *Bm* Bridgeman method, *MA* mechanical alloying, *SSR* solid-state reaction

indicating a constant effective mass and an unaltered valence band maximum. Multiple carrier scattering mechanisms were combined into a clear model that demonstrated how temperature and composition affect mobility [151]. SnTe has been alloyed with MnTe and functions as a significant replacement for thermoelectric PbTe, which contains hazardous Pb. A record peak ZT and a superior average ZT among literature
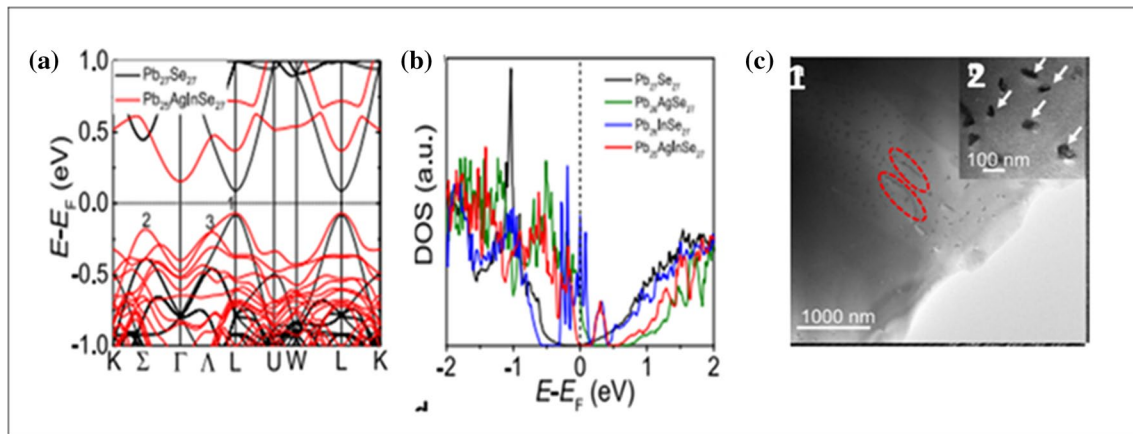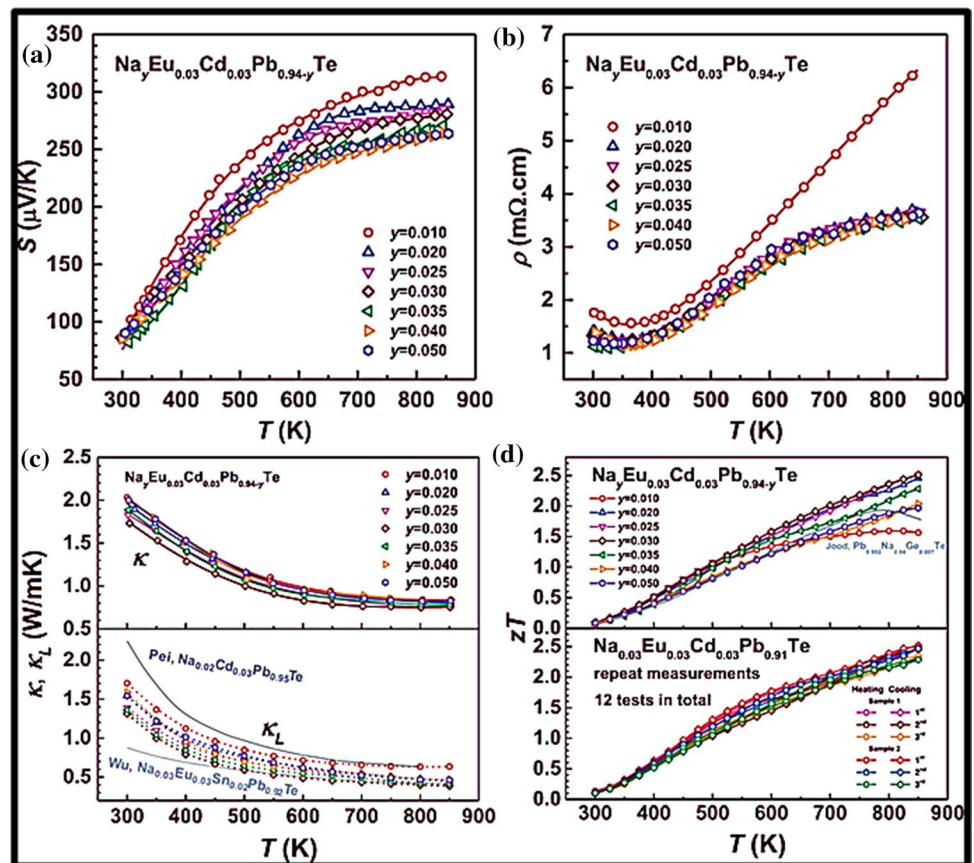
Figure 22 **a** Electronic band structure and **b** DOS **c** TEM images of AgInSe$_2$ added PbSe samples. Reproduced with permission [188]. Copyright 2022, Springer nature.

Figure 23 Thermo-electric properties of Na$_Y$Eu$_{0.03}$Cd$_{0.03}$Pb$_{0.9-y}$ alloy **a** S **b** ρ **c** κ, κ$_l$ **d** ZT. Reproduced with permission [150].

high-performance performance SnTe in the alloy form result from alloying with MnTe up to 15% mol. Both the band structure for a power factor enhancement and the phonon scattering for a reduction in lattice thermal conductivity is improved [152]. Yingcai Zhu

et al. demonstrated the addition of AgInSe$_2$ to p-type PbSe allows for the simultaneous understanding of multiple valence band and strong phonon scattering. Large weighted mobility is made possible by the numerous valley, indicating improved electrical

properties. Strong phonon scattering brought on by numerous nano-scale precipitates and dislocations leads to extremely low lattice thermal conductivity. As a result, they obtained a remarkable ZT of 1.9 at 873 K in p-type PbSe. They showed that by adjusting the composition, it is possible to achieve a combination of band manipulation and microstructure engineering, which is anticipated to be a common method for enhancing thermoelectric performance. To figure out the origin of the enhanced Seebeck coefficient, DFT calculations were made. With the incorporation of AgInSe$_2$ in the PbSe matrix, they noticed a significant change in the electronic band structure (Fig. 22a). Doping causes the bandgap to widen, which reduces the bipolar effect and makes it easier to increase the Seebeck coefficient. According to DFT results, the incorporation of Ag is primarily responsible for the enlarged bandgap. Ag and Se have a greater difference in electronegativity (0.62) than Pb and Se (0.22). Ag will therefore increase the charge transfer between the cation and anion at Pb sites, resulting in a wider bandgap. It's interesting to note that Na doping increases the bandgap to about 0.38 eV. The L band is also made

flatter. The band flattening character is also revealed by the sharp peaks reflected in the density of states (DOS) for the valence band (Fig. 22b). The energy offset (ΔE1-2) between the L and Σ bands is shortened simultaneously as the band is elevated. Surprisingly, the Λ point activates a third valence band that maintains the same energy level as the Σ band (Fig. 22a). The increased Seebeck coefficient and the weighted mobility are the result of these multiple valence bands' ability to provide a large effective mass without significantly affecting carrier mobility [149]. According to the TEM images of the PbSe sample (Fig. 22C(1,2)), the PbSe matrix contains numerous nanoscale precipitates. Strip-like dislocations are additionally seen (Fig. 22 c(1)'s circled regions). Both multiscale dislocations and nanoscale precipitates function as efficient phonon scattering centers. The strong phonon scattering caused a significant reduction in the lattice thermal conductivity of the sample, bringing it to its amorphous limit of 0.31 W m^{-1} K^{-1} at 873 K. This will lead to a ZT of 1.9. Some of the mid-temperature materials alloyed with different elements and their thermoelectric figure of merit, ZT are listed in Table 3 (Fig. 24).
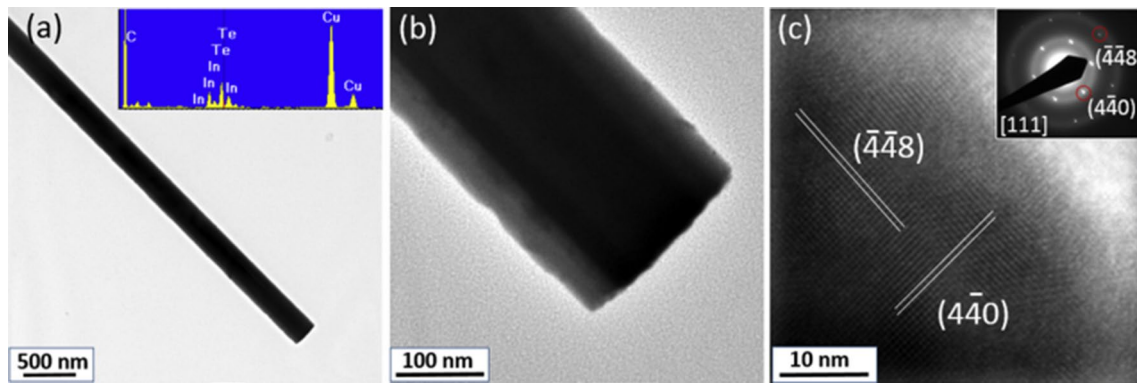

Figure 24 **a** TEM image of the In$_2$Te$_3$ nanowire with EDS spectrum data **b** High-magnification TEM image of the nanowire, **c** HRTEM image of the In$_2$Te$_3$ nanowire. Reproduced with permission [162]. Copyright 2019, Materials Research Bulletin.

Table 3 List of some mid-temperature materials alloyed with different elements and their thermoelectric figure of merit, ZT

Sl.No	Material	Type	Method	Alloyed with	ZT	T (K)	Refs.
1	Cl doped PbS	*n*	M	Bi	0.8	823	[154]
2	PbTe	*p*	A	EuTe and CdTe	2.5	850	[150]
3	PbTe	*p*	HP	CdTe	1.7	700–800	[149]
4	PbSe	*n*	M + SPS	CdSe	1.4	873	[155]
	PbSe	*p*	M + A	SrSe	0.8	813	[156]
5	SnSe	*p*	M + A + SPS	PbSe	0.85	800	[151]
6	SnTe	*p*	M + Q + A	MnTe	1.3	900	[152]
7	SnSe	*p*	SPS	SnS	1.2	793	[157]

Nanostructuring

The idea of "nanostructuring" describes how materials are structured and constrained in size at the nanoscopic level. By introducing nanometer-sized polycrystalline and interfaces into bulk materials, nanostructured thermoelectric materials are intended to increase phonon scattering and decrease lattice thermal conductivity [158]. Because of their outstanding thermoelectric performances, nanostructured materials become the most potential candidates for commercial use among different types of thermoelectric materials. Because the density of states (DOS) near the Fermi level can be improved through quantum confinement, resulting in an increase in thermopower. Because phonons over a wide range can be effectively scattered by a high density of interfaces, resulting in a decrease in the lattice thermal conductivity. The low-dimensional thermoelectric materials are thought to have greater thermoelectric properties than their bulk counterparts. There is an effective increment in the ZT value can be found in 1D and 2D thermoelectric materials [114]. Hicks and Dresselhause are the first to propose theoretically the high ZT value by nanostructure engineering in 1993 [159]. Their model suggested that increasing the Seebeck coefficient and decreasing thermal conductivity due to phonon scattering at the interfaces would improve ZT. Quantum well and superlattice structures (2D TE materials): Better thermoelectric devices may be made with quantum dot superlattice (QDSL) structures, which have a delta-function distribution of density of states and discrete energy levels as a result of three-dimensional quantum confinement, a potentially more advantageous carrier scattering mechanism, and a drastically reduced lattice thermal conductivity. Harman et al. developed quantum-dot superlattices in the PbTe-PbSeTe system, described as PbSe nanodots embedded in a PbTe matrix and showed ZT = 1.6, which is significantly higher than their bulk counterparts (ZT = 0.34) [160]. This work was motivated by the prediction that quantum confinement may lead to an increased Seebeck coefficient and therefore higher ZT. According to Rogacheva et al [161]. the n-PbTe/p-SnTe/n-PbTe heterostructures' thermoelectric properties depend on the SnTe quantum well width in a distinct nonmonotonic manner. It is reported that the maximum thermoelectric power factor corresponds to $d_{SnTe} = 2.5$ nm and that the results are understood based on a size quantization of the energy spectra in the SnTe QW. As phonons

can be scattered by the interface between layers, the layers may decrease the phonon thermal conductivity and as a result, ZT has increased. Nanowires (1D TE materials): Due to stronger phonon scattering and quantum confinement compared to two-dimensional counterparts, quantum nanowires may have a greater improvement in thermoelectric performance. Furthermore, it has been suggested that the additional phonon scattering on the inner and outer surfaces of nanotubes makes them have lower lattice thermal conductivity than nanowires [114]. As shown in Fig. 25d in the case of the In_2Te_3 nanowire the maximum reported ZT value is about 1.8 at 300 K and by observing Fig. 25 a and c we can conclude that as temperature increases the Seebeck coefficient and resistivity decreases. Maximum Seebeck co-efficient is reported as 72μv/K and resistivity is about ~ 26mΩ.cm at 300 K, but the total thermal conductivity was found to increase with increasing temperature, and it is minimum at 300 K as shown in Fig. 25b. By observing TEM and HRTEM images, Fig. 24b is a comparatively smooth surface compared to that of etched Si nanowires; this suggests that the effect of the surface roughness on the thermal conductivity will not be significant, Fig. 24a–c shows the TEM and HRTEM images of the samples [162]. Some of the mid-temperature nanostructured materials and their thermoelectric figure of merit, ZT are listed in Table 4.

Nanocomposites

The low-dimensional material systems are currently being put together as nanocomposites, which consist of an assembly of nanoclusters that exhibit short-range low dimensionality and are embedded in a host material. This creates a bulk material with nanostructures and numerous interfaces that scatter phonons more effectively than electrons [171]. The next logical step for extending the success of nanostructures to more scalable material is nanocomposites with reduced thermal conductivity by interface scattering. A promising method for creating bulk samples with nanostructured constituents is provided by nanocomposite thermoelectric materials. From the perspective of material characterization and property measurement, such nanocomposite materials are simple to work with. Phase interfaces are produced when material dimensions are reduced to the nanometer level, and they are crucial for improving the properties of the material. Knowing the connection between structure

Figure 25 Thermoelectric properties of In_2Te_3 nanowires **a** ρ **b** κ **c** S **d** ZT. Reproduced with permission [162]. Copyright 2019, Materials Research Bulletin.
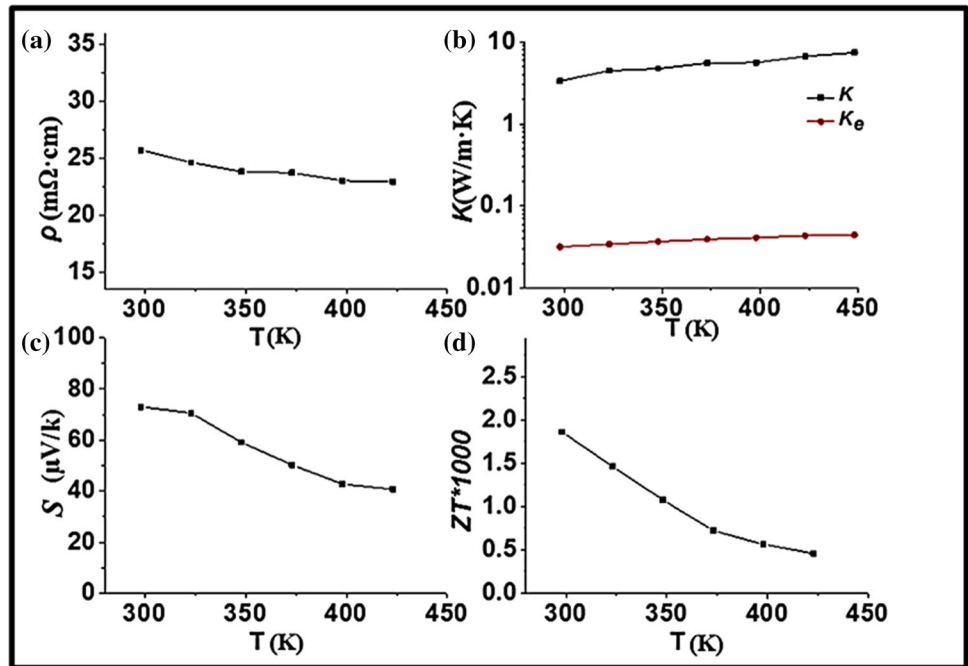

Table 4 List of some mid-temperature nanostructured materials and their thermoelectric figure of merit, ZT

Sl.No	Material	Type	Method	ZT	T (K)	Refs.
1	Nanostructured $In_XSn_{1-X}Te$	p	BM + HP	1.1	873	[121]
2	PbSeTe-based quantum dot superlattice	n	MBE	2.0	300	[160]
3	SnTe nanosheets	p	Ion-exchange reaction	1.1	923	[163]
4	SnTe nanocrystals	p	MHT	0.49	803	[164]
5	Nanostructured PbS	n	VT + BM	0.94	710	[165]
6	2D-$SnSb_2Te_4$	p	DFT	2.6–5.5	300–750	[166]
7	2D-$PbSb_2Te_4$	p	DFT	0.7–2.2	300–750	[166]
8	2D-$PbBi_2Te_4$	p	DFT	1.6–4.2	300–750	[166]
9	Se quantum dot/Nanostructured SnSe	p	HT	2.0	873	[167]
10	SnS nanosheets	p	Li-intercalation and exfoliation	0.078	450	[168]
11	In doped SnTe nanowires	p	VD	0.07	300	[169]
12	In_2Te_3 Nanowires	p	TCVD	1.8	300	[162]
13	2D InTe	n	DFT	2.7	300	[170]

The abbreviations listed in the column for the synthetic technique stand for the following ideas: *MBE* Molecular-beam epitaxy, *VT* vapour transport, *VP* vapour deposition, and *TCVD* Thermal chemical vapor deposition, *MHT* Microwave Hydrothermal method

and property directly depends on the ratio of reinforced material volume to the surface area used in the preparation of nanocomposite materials [172]. Maria et al. synthesized PbTe-PbS nanocomposites by bottom-Up approach of functional nanocomposites using core–shell nanoparticles as building blocks and they reported the ZT of 1.1 at 710 K. This report provided a reason for the lower thermal conductivities by pointing to the partial phase alloying, incoherent interfaces,

and mismatched acoustic impedances of the PbTe and PbS phases [173]. Yim et al. investigated the thermoelectric properties of Indium-Selenium nanocomposites synthesized by utilizing mechanical alloying and spark plasma sintering. They also demonstrated that the prepared samples displayed n-type conductivity at room temperature, with Seebeck coefficients ranging from −159 to −568 µV K^{-1}. To further improve the thermoelectric figure of merit in In-Se-based compounds,

the electrical conductivity can be increased without affecting the Seebeck coefficient, and the thermal conductivity is reduced by increasing phonon scattering with boundaries, which will induced by nanoscaled particles, the boundaries regions [174]. Lisi Huang et al. showed that SnSe/rGO nanocomposites were synthesized in situ using a simple, one-step bottom-up solution process and they specifically mentioned that the nanocomposite method helps to enhance the electrical conductivity over the low-temperature range due to increased carrier concentration and significantly lowering the material's lattice thermal conductivity, which can be attributed to enhanced phonon scattering from high-density SnSe/rGO interfaces [175]. Figure 26 depicts the temperature dependence of the prepared composite's TE properties (α, σ, κ, and

ZT). When evaluating TE properties, the highest ZT value 1.2 is obtained at 750 K as shown in Fig. 26d. The conductivity is more in pristine sample compared to the composties as shown in Fig. 26b. The maximum value of Seebeck coefficient was found to increase to 240 $\mu v/K$ as temperature increases from room temperature to 750 K in case of X = 0.5 composite sample is shown in Fig. 26a. Due to its larger Seebeck coefficient, PF in the composite samples is higher than the pristine sample in the temperature range of 300–750 K. However, low thermal conductivity was found to be 2.44 W m^{-1} K^{-2} at 750 K for X = 0.5 composite sample, as shown in Fig. 26c. Some of the mid-temperature nanocomposite materials and their thermoelectric figure of merit, ZT are listed in Table 5.
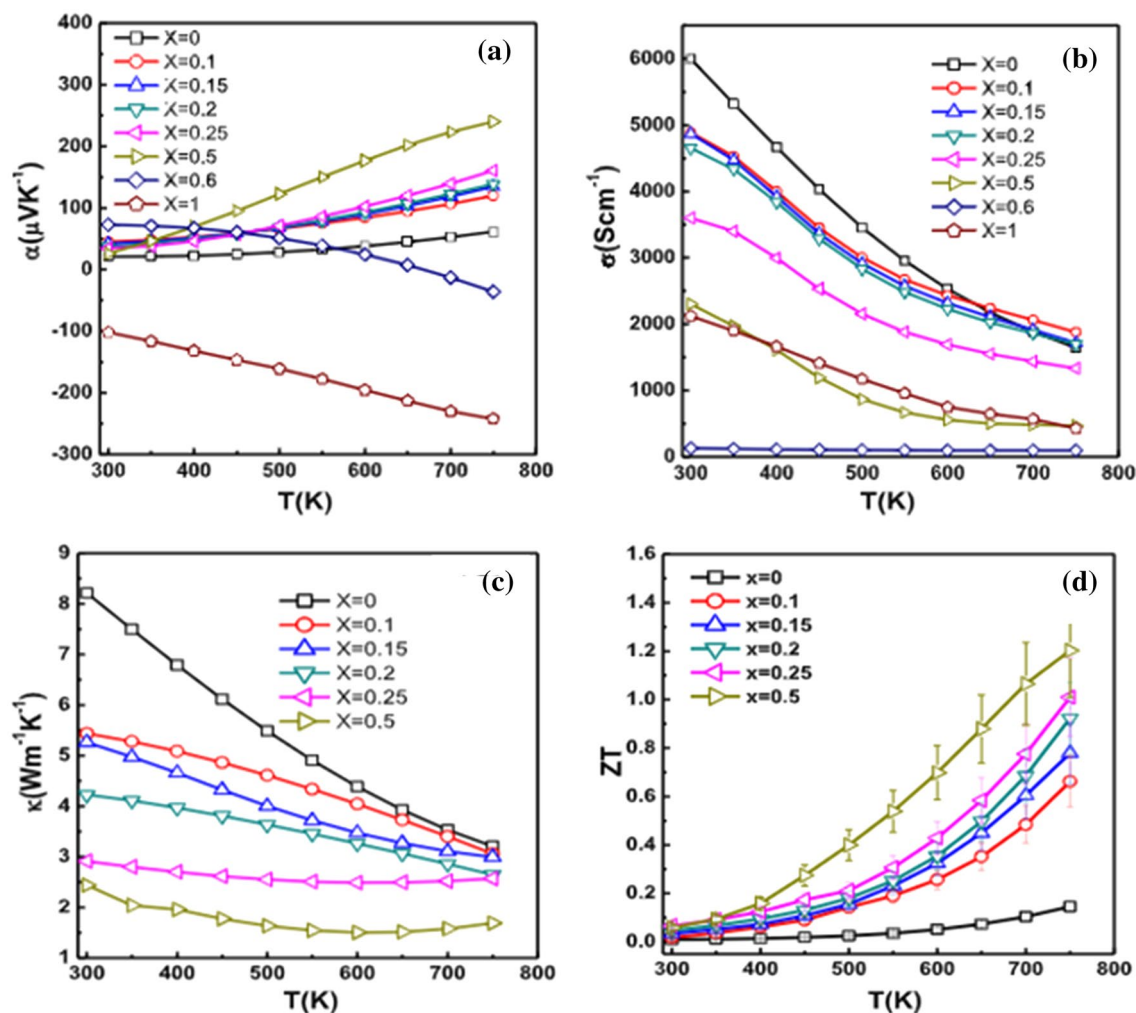

Figure 26 Thermoelectric properties of SnTe/PbTe$_4$ composites **a** ρ **b** α **c** κ **d** ZT [190]. Reproduced with permission. Copyright 2020, ACS.

Table 5 List of some mid-temperature nanocomposite materials and their thermoelectric figure of merit, ZT

| Sl.No	Material	Type	Method	ZT	T (K)	Refs.
1	PbSe-Ag	p	Bottom-up (Solution processed)	0.97	723	[176]
2	BST/PbSe	p	M + BM + S	1.56	400	[177]
3	PbTe	p	M + Q + HP	2.0	773	[178]
4	PbTe/graphene	n	Wet chemical method	0.7	670	[179]
5	PbS/Ag	n	Bottom-up	1.7	850	[60]
6	PbTe/PbS	n	M + A	0.76	573	[180]
7	PbTe/PbS	n	NP	1.4	750	[181]
8	PbTe/Si	n	NP	0.9	675	[182]
9	SnSe/Ag_2Se	p	BM + SPS	0.74	773	[183]
10	Cl doped $SnSe_2$/SnSe	n	M + Q	0.56	773	[184]
11	SnS/SnO	p	Polyol method	0.0036	325	[185]
12	SnTe	p	M + Q	1.02	873	[186]
13	SnSe/PbTe	p	M + BM + HP	1.26	880	[187]
14	$CuInTe_2$/SnTe	p	Cation exchange	1.68	823	[188]
15	SnTe/PbS	p	SPS	0.8	873	[189]
16	SnTe/PbTe	p	M + BM + A	1.2	750	[190]
17	In-Se	n	MA + SPS	0.84	673	[174]
18	In-Se/$SrTiO_3$	n	SSR	0.21	600	[191]
19	InSe/In_4Se_3	n	SSR	0.25	600	[191]
20	In_4Se_3-In	n	ZM	0.9	700	[192]

The abbreviations listed in the column for the synthetic technique stand for the following ideas: *ZM* zone melting, *NP* nano precipitation

To sum up, improving thermoelectric efficiency is essential for the creation of thermoelectric materials and modules. Numerous methods, such as nanostructuring, doping, and composite materials, have been suggested to increase the effectiveness of thermoelectrics. Researchers have been able to significantly enhance the thermoelectric performance of materials by applying these techniques. Additionally, it has been demonstrated that a synergistic combination of several strategies can increase efficiency even further. Maximizing thermoelectric efficiency, however, requires a thorough understanding of material properties, device design, and manufacturing procedures. The development of high-efficiency thermoelectric material is crucial despite these obstacles because it could lead to the creation of a sustainable energy source for a variety of applications.

Some of the growth techniques mentioned in Sect. "Strategies to optimize thermoelectric performance", are schematically shown in Fig. 27.

Drawbacks of mid-temperature range chalcogenide-based thermoelectric materials

There are several drawbacks associated with mid-temperature range thermoelectric materials. Limited efficiency: Although mid-temperature range thermoelectric materials has improved efficiency compared to low-temperature materials, they still fall short in comparison to high-temperature thermoelectrics. Cost: The production of mid-temperature range thermoelectric materials is typically more expensive than low-temperature materials because of the requirement of complex processing and manufacturing methods like the Bridgeman method [193]. Material availability: Mid-temperature range thermoelectric materials are less abundant than low-temperature materials, which can limit their availability. Stability:
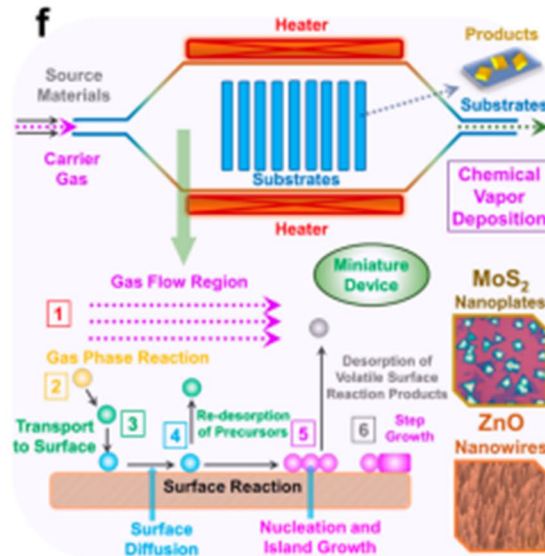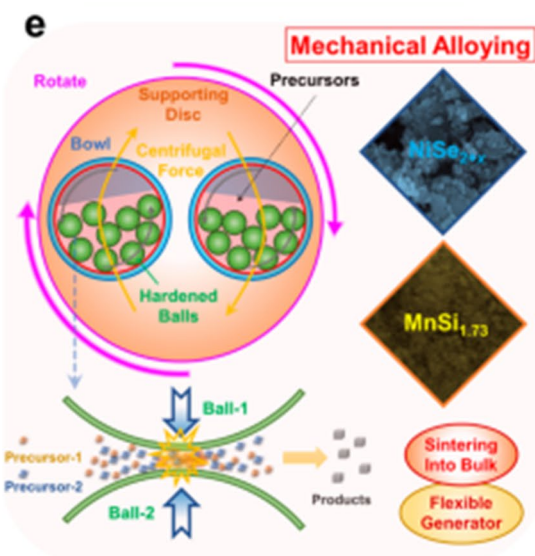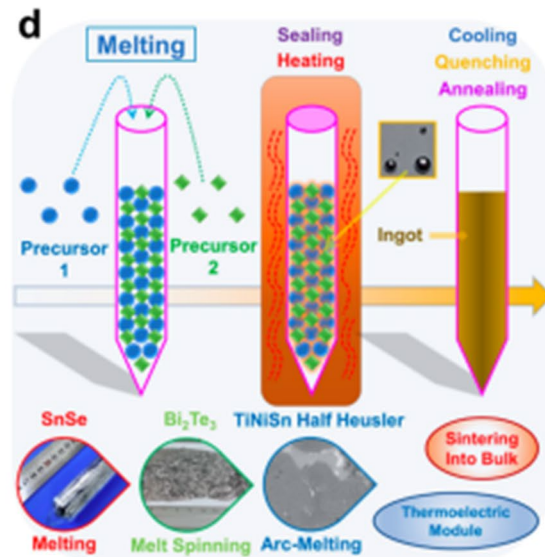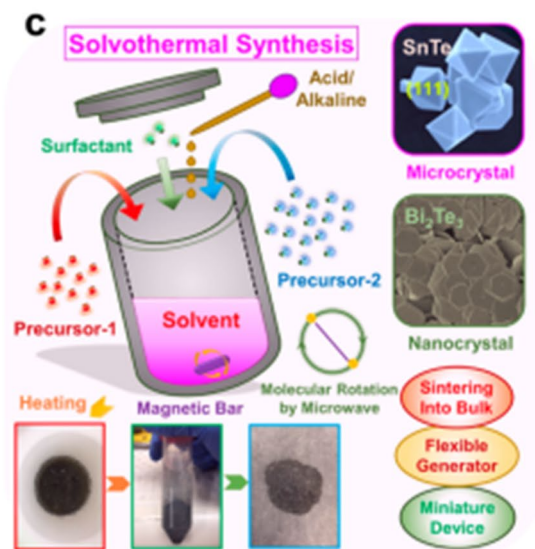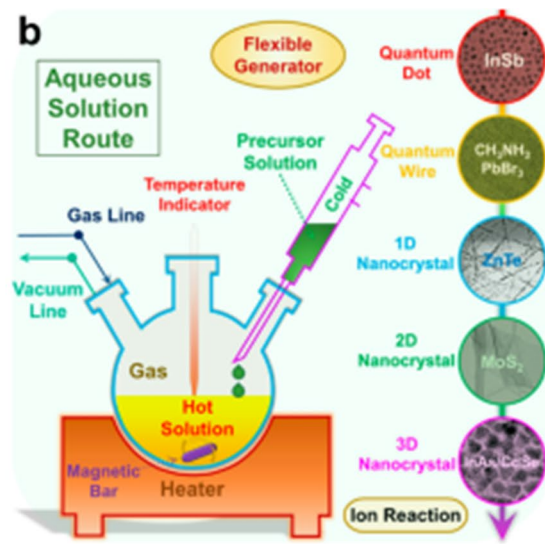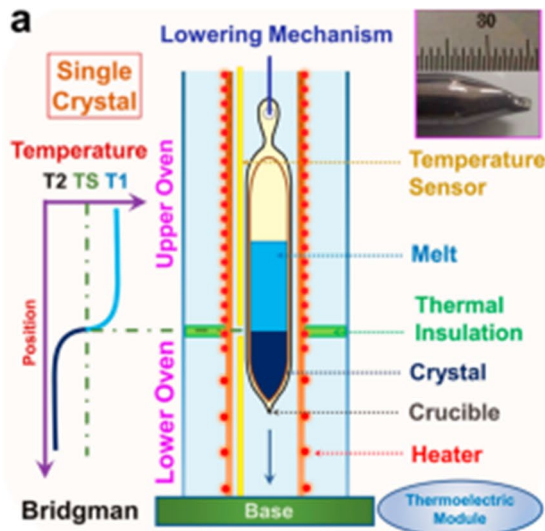
◄**Figure 27** Schematic diagrams of techniques used to synthesize the samples **a** Bridgeman method **b** Aqueous solution synthesis method **c** Hydro-solvothermal synthesis **d** elting method **e** Mechanical alloying method **f** Chemical vapour deposition method [5]. Reproduced with permission. Copyright 2020, American chemical society.

Mid-temperature range thermoelectric materials may experience performance degradation over time, especially when subjected to high temperatures or stress. Performance variability: The performance of mid-temperature range thermoelectric materials can vary greatly depending on the material used the and manufacturing process, leading to difficulties in ensuring consistent performance. These are general drawbacks of mid-temperature range thermoelectric materials.

Will discuss the drawbacks of each series specifically, Lead Chalcogenides (such as PbS, PbSe, and PbTe) are widely studied mid-temperature range thermoelectric materials. Some specific drawbacks associated with these materials include Toxicity: Lead is a toxic element and its presence in thermoelectric materials raises concerns about the environmental impact of their use and disposal [194]. Instability: Lead Chalcogenides are prone to phase transitions and structural changes, which can negatively impact their thermoelectric performance. Low thermal conductivity: Lead Chalcogenides have relatively low thermal conductivity, which can limit their efficiency as thermoelectric materials. High cost: The production of Lead Chalcogenides can be expensive, which may limit their adoption in commercial applications. Limited mechanical stability: Lead Chalcogenides can be brittle and prone to cracking, which can make them challenging to use in applications where mechanical stress is a concern.

Tin Chalcogenides (such as SnS, SnSe, and SnTe) and Indium Chalcogenides (such as InS, InSe, and InTe) are promising mid-temperature range thermoelectric materials. Some specific drawbacks associated with these materials include Synthesis difficulties: Tin Chalcogenides can be challenging to synthesize with high purity and uniform composition, which can negatively impact their thermoelectric performance. Limited stability: Tin Chalcogenides are prone to phase transitions and structural changes, which can negatively impact their thermoelectric performance over time. Poor mechanical stability: Tin Chalcogenides can be brittle and prone to cracking, which can limit their use in applications where mechanical stress is a

concern. High cost: The production of Tin Chalcogenides can be expensive, which may limit their adoption in commercial applications.

In Sect. "Strategies to optimize thermoelectric performance", various strategies for strengthening the thermoelectric abilities of typical medium-temperature thermoelectric materials like PbTe, PbSe, PbS, SnSe, SnS, SnTe, InSe, InS, and InTe have been discussed. The strategies include electrical transport optimization, thermal conductivity reduction, band structure tailoring, defect management, and material-specific approaches. These optimization strategies were designed to address and mitigate the drawbacks associated with these materials. Each of these materials presents unique challenges and addressing their specific drawbacks is key to improving their thermoelectric efficiency. Despite these drawbacks, mid-temperature range thermoelectric materials hold great potential as a promising alternative to high-temperature thermoelectrics, especially in applications where high-temperature materials are not feasible. To overcome these challenges, further research is needed to improve the efficiency, stability, and scalability of mid-temperature range thermoelectric materials.

## Applications of mid-temperature range chalcogenide-based thermoelectric materials

Mid-temperature range chalcogenide-based thermoelectric materials have a broad range of applications across various fields due to their ability to efficiently harness waste heat, generate power from temperature gradients, and provide precise thermal control. Some general applications of thermoelectric materials such as, waste heat recovery: One of the most significant applications of thermoelectric materials is in capturing and converting waste heat from industrial processes, power plants, and vehicle exhaust into electricity. This can improve energy efficiency and reduce greenhouse gas emissions. Portable power generation: Thermoelectric generators (TEGs) can be used in remote or off-grid locations to power sensors, communication devices, and other small electronic devices, such as in military operations, environmental monitoring, and wilderness exploration. Automotive: Thermoelectric generators can help to improve the fuel efficiency of vehicles by converting some of the waste heat from the engine into electricity, which can be

used to charge the vehicle's battery or power auxiliary systems. Aerospace: In aerospace applications, thermoelectric materials can be utilised for power generation in satellites, spacecraft, and space probes. Electronics Cooling: Thermoelectric coolers (TECs) are used to control the temperature of electronic components and semiconductor devices. They can be used as either heat source or heat sink for precise thermal management applications. Medical Devices: Thermoelectric devices are used in medical applications, such as temperature control for laser systems, portable refrigeration for vaccines and medications, and temperature regulation for laboratory equipment. Wearable Technology: Thermoelectric generators can be integrated into wearable devices to harvest body heat and extend the battery life or power low-energy sensors and components. Industrial Processes: They can be used for maintaining specific temperatures in industrial processes, such as in chemical reactors and furnaces. Solar Power: In concentrated solar power (CSP) systems, thermoelectric materials can be employed to convert high-temperature heat from solar collectors into electricity. Consumer Electronics: Some consumer electronic devices, such as camping stoves

with USB chargers, use thermoelectric generators to charge small electronic devices. Combined Heat and Power (CHP) Systems: Mid-temperature thermoelectric generators can be used in paired heat and power systems, to simultaneously produce electricity and useful heat for residential, commercial, and industrial applications. Thermal Batteries: Mid-temperature thermoelectric materials can be incorporated into thermal batteries for energy storage, allowing for the storage of excess heat and its conversion back into electricity when needed. These are some general applications of mid-temperature range chalcogenide-based TE materials and are illustrated in Fig. 28.

The research conducted over the decades has shown that nanostructured metal chalcogenides are the most significant materials for designing high-performance energy conversion and storage devices, as well as for detecting impurities in gas and aqueous media, and for biomedical applications [55]. The potential use of lead-based chalcogenides, PbTe, PbSe, and PbS, as thermoelectric energy converters and electronic devices, has led to the extensive experimental study of these materials over the past few decades [36]. PbTe has been extensively studied

Figure 28 General applications of mid-temperature range chalcogenide-based TE materials.
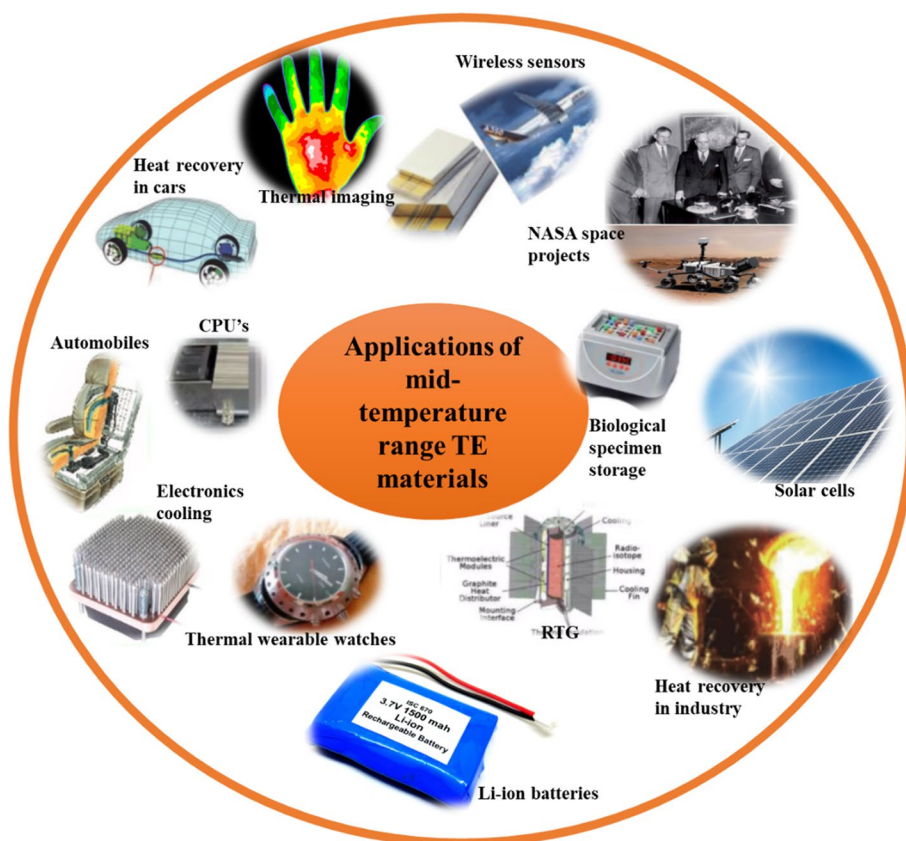
as a thermoelectric material since 1950s, under the direction of Ioffe in the Soviet Union and Fritts at the US-based 3 M corporation. PbTe's traditional uses include power generation for space mission applications such as NASA space mission with ZT ~ 0.8 [149]. It is additionally utilized in steel metallurgy, solar cells, and phase change materials for digital recording, among many other things [51]. PbS is a prominent narrow-band-gap semiconductor. It is employed in a variety of devices, which include photodetectors with a wide range of wavelengths from infrared (IR) to ultraviolet (UV), high-efficiency solar cells, thermoelectric transducers, as well as optical switches [55]. PbSe's infrared behavior has been studied since 1940s and it has found various applications in photodetectors and thermal imaging. The invention of nanoscience has recently boosted attention to photovoltaic applications [16].

Indium selenides with layer structures, such as $In_4Se_3, \alpha/\beta$-In_2Se_3, and β/γ-InSe, have received a lot of attention over the past few decades because of their potential use in thermoelectrics, solar cells, Li-ion batteries, photodetectors, and memory devices. In_4Se_3 forms a layered structure of $(In_3)5^+$ multivalent groups bonded to Se ions, whereas α/β-In_2Se_3 and β/γ-InSe form atomic layers of Se-In-Se-In-Se and Se-In-In-Se, respectively. Anisotropic bonding properties, such as intense intralayer covalent bonding as well as weak interlayer van der Waals interactions, result in highly anisotropic optical, electrical, and thermal properties. Because of their anisotropic photon structures and large surface-to-volume ratios, as well as photon and carrier confinement effects, layered indium selenide nanomaterials are expected to have superior physical properties [83]. Due to its high bandgap, indium sulfide has potential uses such as photoconductive, Photoluminescence materials and high-performance solar cells [195]. Indium tellurides are commonly used in electronics as well as optical capturing mechanisms or instruments. In_2Te_5 is a Penta telluride member, serves as a layered semiconductor with a bandgap of 0.88–1.26 eV [81]. Early studies only reported on the bulk's crystal structure, electric conductivity, and thermoelectric power. Additionally, both experimental and theoretical research reveals anisotropy in the thermal conductivity of In_2Te_5. Given the character of the in-plane anisotropic crystal structure, In_2Te_5 could show a variety of anisotropic physical properties and find use in feasible optoelectronic and electronic devices with distinct anisotropic properties [81].

Because of its unique properties such as direct band gap, large absorbability, adjustable electrical properties, thermal as well as chemical stability, and layered structure, SnS semiconductor is a potentially beneficial material for a wide range of applications, such as photovoltaics, optoelectronics, chemical sensors, solid-state batteries, holographic, photoelectrochemical cells, lithium-ion batteries, infrared detectors, and so on [105]. Tin selenide has a direct bandgap, which can absorb and emit light efficiently. This property makes it an ideal material for optoelectronic applications, such as solar cells, photodetectors, and light-emitting diodes (LEDs). Tin Selenide has been used in energy storage devices like lithium-ion batteries, due to its high electrical conductivity and stability [94]. It is also used in spintronics which is a technology that uses the spin of electrons to store and process information as well as in wearable electronics and to convert solar energy into electricity and used in phase-change memory devices, super capacitors, rechargeable batteries, photovoltaic fields, and topological insulator [196]. SnTe has excellent thermoelectric properties and can be used in thermoelectric generators to convert waste heat into electricity, used in solar cells because of its high absorption coefficient in the visible and near-infrared regions of the electromagnetic spectrum, making it a promising candidate for use in thin-film solar cells, and also used in optoelectronic devices such as light-emitting diodes (LEDs), photodetectors [197]. The extreme anharmonicity of chemical bonds within the SnSe layered compound is responsible for the extremely low κ, which is only 0.35 Wm^{-1} K^{-1} at 923 K. As a result, SnSe represented a significant advancement for the thermoelectric community and provided direction for the investigation and development of high-efficiency thermoelectric materials [198].

Outlook for future direction

This review has clarified the status of chalcogenide-based thermoelectrics and their potential; these materials provide both opportunities and difficulties, furthermore, it draws attention to the fact that thermoelectric engineering and science are entering a dynamic new era. The future of this technology will be shaped by a convergence of knowledge in the domain of materials science, thermoelectric device engineering, and system integration as researchers, engineers, and innovators set out on this journey through the

fusion of innovation, sustainability, and practicality. As research progresses, material scientists and engineers continue to explore novel materials with advanced synthesis techniques, and cutting-edge characterization methods. The goal is to optimizing mid-temperature thermoelectric materials in terms of Seebeck co-efficient, power factor and thermoelectric figure of merit (ZT) and addressing practical concerns such as material cost and environmental impact and overcoming their inherent drawbacks. Mid-temperature thermoelectric materials may play vital role in fulfilling the growing energy demand for effective and sustainable energy solutions in industries, automobiles, the medical field, defense, etc.

Conclusions

This paper provides a review of mid-temperature thermoelectric materials along with the advancements made in thermoelectric performance measurements. It provided a discussion on several techniques, such as doping, co-doping, alloying, nanostructuring, and nanocompositing that have been employed to improve their thermoelectric properties. Due to the alteration of the electron density as well as the scattering of carriers along with phonons by the defects induced, doping and alloying have been demonstrated to be effective in improving power factor and reducing thermal conductivity. Additionally, ZT is enhanced by nanostructuring into various nano-shaped forms. The power factor is raised by low-energy carrier filtering, whereas thermal conductivity is decreased by phonon scattering at interfaces. Chalcogenide-based mid-temperature thermoelectric materials are found to be very promising when compared to other conventional thermoelectric materials. Because of a reduction in structural dimensions, the thermoelectric response of PbX (X = Se, Te, S) monolayers has significantly improved. The narrow bandgaps and large density of states (DOS) that correspond to the bandgap edges are the reasons for the improvement in the thermoelectric response. As a result, the large Seebeck coefficients and high electrical conductivities were simultaneously obtained, resulting in significant thermoelectric PF and ZT at room temperature. When compared to the ZT values of 0.48, 0.45, and 0.30 obtained for bulk PbS, PbSe, and PbTe, respectively, at 723 K, a ZT value of 1 for PbX monolayers at room temperature is noticeably better. SnSe challenges recognized standards to

identify a promising thermoelectric material because it is made up of light elements and has a small, basic unit cell. Without optimizing the carrier concentration, the record high ZT of 2.6 at 923 K for single crystals of SnSe along the b-axis was attained leading to a moderate power factor of 8.5 Wcm^{-1} K^{-2} at 923 K. We still have several problems to resolve before we can develop a high-performance thermoelectric module based on tin chalcogenide. Despite being a homolog of PbTe, thermoelectrics researchers were unable to achieve the same high ZT in SnTe, which suggests that there are a lot of unexplored opportunities for future research. In SnTe thermoelectrics, high p-type carrier optimization is still difficult. Despite the fact that research on the thermoelectric properties of In$_4$Se$_3$ has recently begun, ZT improvements have been impressive, with ZT values of 1.53 and 1.4 for single crystals as long as polycrystalline materials, respectively. The maximum ZT of 0.6 in In$_2$Se$_3$ and InSe-based thermoelectric materials have been achieved due to their low thermal conductivity. Power factor improvement is the main concern for their ZT enhancement. Developing effectively doped structures without altering the crystal structure is a key tactic for increasing their power factor. The main barriers to achieving high ZT for In$_3$Se$_4$ nanostructured materials are the low carrier concentration and electrical conductivity. In$_3$Se$_4$ can obtain increased carrier concentration and electrical conductivity through optimum doping, which can then result in a reasonable ZT, by altering its electronic structure. This review summarizes the state of knowledge regarding lead chalcogenides, indium chalcogenides, and tin chalcogenides belonging to mid-temperature range thermoelectric materials. It summarizes structural features, strategies to improve ZT, thermoelectric properties, drawbacks, and applications of materials in every aspect. There have been several ideas put forth for improving their thermoelectric properties, but even more, studies are needed to improve the thermoelectric performance of mid-temperature chalcogenide-based thermoelectric materials.

Acknowledgements

Author contributions

MRS: Conceptualization, visualization, writing the original draft. ANP: Supervision, validation, writing-review, and editing.

Funding

Data and code availability

Not applicable.

Declarations

Conflict of interest The authors confirm that they have no known financial or interpersonal conflicts that might have appeared to have influenced the research presented in this paper.

Ethics approval Not applicable.

References

[1] Bull SR (2001) Renewable energy today and tomorrow. Proc IEEE 89(8):1216–1226. https://doi.org/10.1109/5.940290

[2] Han G, Chen ZG, Drennan J, Zou J (2014) Indium selenides: structural characteristics, synthesis and their thermoelectric performances. Small 10(14):2747–2765. https://doi.org/10.1002/smll.201400104

[3] Alsalama MM, Hamoudi H, Abdala A, Ghouri ZK, Youssef KM (2020) Enhancement of thermoelectric properties of layered chalcogenide materials. Rev Adv Mater Sci 59(1):371–378. https://doi.org/10.1515/rams-2020-0023

[4] Zheng JC (2008) Recent advances on thermoelectric materials. Front Phys China 3(3):269–279. https://doi.org/10.1007/s11467-008-0028-9

[5] Shi XL, Zou J, Chen ZG (2020) Advanced thermoelectric design: From materials and structures to devices. Chem Rev 120(15):7399–7515. https://doi.org/10.1021/acs.chemrev.0c00026

[6] Drebushchak VA (2008) The Peltier effect. J Therm Anal Calorim 91(1):311–315. https://doi.org/10.1007/s10973-007-8336-9

[7] Du CY, da Wen C (2011) Experimental investigation and numerical analysis for one-stage thermoelectric cooler considering Thomson effect. Int J Heat Mass Transf 54(23–24):4875–4884. https://doi.org/10.1016/j.ijheatmasstransfer.2011.06.043

[8] Rowe EDM, D. Ph, D. Sc, and F. Group, *HANDBOOK*. 2006.

[9] Choi YH et al (2012) Simple tuning of carrier type in topological insulator Bi_2Se_3 by Mn doping. Appl Phys Lett 101(15):152103(1)–152103(4). https://doi.org/10.1063/1.4755767

[10] Ashalley E, Chen H, Tong X, Li H, Wang ZM (2015) Bismuth telluride nanostructures: preparation, thermoelectric properties and topological insulating effect. Front Mater Sci 9(2):103–125. https://doi.org/10.1007/s11706-015-0285-9

[11] Bai Y et al (2023) Boosting the thermoelectric performance of n-type Bi_2S_3 by compositing rGO. J Alloys Compd 933:1–11. https://doi.org/10.1016/j.jallcom.2022.167814

[12] Kim M, Park D, Kim J (2023) Self-healing boron-doped Sb_2Se_3 thermoelectric materials prepared using liquid metallic Ga–Sn alloys. J Mater Sci 58(22):9251–9263. https://doi.org/10.1007/s10853-023-08593-2

[13] Qin H et al (2020) Achieving a high average zT value in Sb_2Te_3-based segmented thermoelectric materials. ACS Appl Mater Interfaces 12(1):945–952. https://doi.org/10.1021/acsami.9b19798

[14] Nasr TB, Maghraoui-Meherzi H, Kamoun-Turki N (2016) First-principles study of electronic, thermoelectric and thermal properties of Sb2S3. J Alloys Compd 663:123–127. https://doi.org/10.1016/j.jallcom.2015.12.093

[15] Falkenbach O, Hartung D, Klar PJ, Koch G, Schlecht S (2014) Thermoelectric properties of nanostructured bismuth-doped lead telluride $Bi_x(PbTe)_{1-x}$ prepared by co-ball-milling. J Electron Mater 43(6):1674–1680. https://doi.org/10.1007/s11664-013-2832-4

[16] Androulakis J et al (2011) High-temperature charge and thermal transport properties of the n-type thermoelectric material PbSe. Phys Rev B Condens Matter Mater Phys 84(15):1–11. https://doi.org/10.1103/PhysRevB.84.155207

[17] Li Y et al (2021) Enhanced thermoelectric performance of hot-press Bi-doped n-type polycrystalline PbS. Mater Sci Semicond Process 121:1–10. https://doi.org/10.1016/j.mssp.2020.105393

[18] Zhao LD et al (2016) Ultrahigh power factor and thermoelectric performance in hole-doped single-crystal SnSe. Science 351(6269):141–144. https://doi.org/10.1126/science.aad3749

[19] Moshwan R, Yang L, Zou J, Chen ZG (2017) Eco-friendly SnTe thermoelectric materials: progress and future challenges. Adv Funct Mater 27(43):30–44. https://doi.org/10.1002/adfm.201703278

[20] Han YM, Zhao J, Zhou M, Jiang XX, Leng HQ, Li LF (2015) SnS and SnS-SnSe solid solutiothermoelectric performance ofn. J Mater Chem A Mater 3(8):4555–4559. https://doi.org/10.1039/c4ta06955b

[21] Zhai Y et al (2013) Thermoelectric properties of $In_{1.3-x}Sn_xSe$ prepared by spark plasma sintering method. J Alloys Compd 553:270–272. https://doi.org/10.1016/j.jallcom.2012.11.139

[22] Cho JY, Lim YS, Choi SM, Kim KH, Seo WS, Park HH (2011) Thermoelectric properties of spark plasma-sintered In_4Se_3-In_4Te_3. J Electron Mater 40(5):1024–1028. https://doi.org/10.1007/s11664-010-1492-x

[23] Tabernor J, Christian P, O'Brien P (2006) A general route to nanodimensional powders of indium chalcogenides. J Mater Chem 16(21):2082–2087. https://doi.org/10.1039/b600921b

[24] Guo D et al (2019) The n- and p-type thermoelectricity property of GeTe by first-principles study. J Alloys Compd 810:1–8. https://doi.org/10.1016/j.jallcom.2019.151838

[25] Hao S, Shi F, Dravid VP, Kanatzidis MG, Wolverton C (2016) Computational prediction of high thermoelectric performance in hole doped layered GeSe. Chem Mater 28(9):3218–3226. https://doi.org/10.1021/acs.chemmater.6b01164

[26] Roychowdhury S, Samanta M, Perumal S, Biswas K (2018) Germanium chalcogenide thermoelectrics: electronic structure modulation and low lattice thermal conductivity. Chem Mater 30(17):5799–5813. https://doi.org/10.1021/acs.chemmater.8b02676

[27] Noguchi T (1997) Powder processing of thermoelectric materials—focusing on SiGe with new sintering technique. In: International conference on thermoelectrics, ICT, Proceedings, pp 207–214. https://doi.org/10.1109/ict.1997.667082

[28] Cheikh D et al (2018) Praseodymium telluride: a high-temperature, high-ZT thermoelectric material. Joule 2(4):698–709. https://doi.org/10.1016/j.joule.2018.01.013

[29] Aydemir U et al (2015) Thermoelectric properties of the Zintl phases Yb5M2Sb6 (M = Al, Ga, In). Dalton Trans 44(15):6767–6774. https://doi.org/10.1039/c4dt03773a

[30] Chauhan NS et al (2018) Compositional tuning of ZrNiSn half-Heusler alloys: thermoelectric characteristics and performance analysis. J Phys Chem Solids 123:105–112. https://doi.org/10.1016/j.jpcs.2018.07.012

[31] Zhu T, Liu Y, Fu C, Heremans JP, Snyder JG, Zhao X (2017) Compromise and synergy in high-efficiency thermoelectric materials. Advanced materials 29(14):1–26. https://doi.org/10.1002/adma.201605884

[32] Goldsmid J (2017) The physics of thermoelectric energy conversion. Morgan Claypool Publishers, San Rafael. https://doi.org/10.1088/978-1-6817-4641-8ch2

[33] Culp SR, Poon SJ, Hickman N, Tritt TM, Blumm J (2006) Effect of substitutions on the thermoelectric figure of merit of half-Heusler phases at 800°C. Appl Phys Lett 88(4):1–3. https://doi.org/10.1063/1.2168019

[34] Guo X et al (2016) Effect of doping indium into a Bi2Te3 matrix on the microstructure and thermoelectric transport properties. RSC Adv 6(65):60736–60740. https://doi.org/10.1039/c6ra09767g

[35] Skelton JM, Parker SC, Togo A, Tanaka I, Walsh A (2014) Thermal physics of the lead chalcogenides PbS, PbSe, and PbTe from first principles. Phys Rev B 89(20):1–10. https://doi.org/10.1103/PhysRevB.89.205203

[36] Pei YL, Liu Y (2012) Electrical and thermal transport properties of Pb-based chalcogenides: PbTe, PbSe, and PbS. J Alloys Compd 514:40–44. https://doi.org/10.1016/j.jallcom.2011.10.036

[37] Bauer Pereira P, Sergueev I, Gorsse S, Dadda J, Müller E, Hermann RP (2013) Lattice dynamics and structure of GeTe, SnTe and PbTe. Physica Status Solidi (b) 250(7):1300–1307. https://doi.org/10.1002/pssb.201248412

[38] Ul Haq B et al (2021) Exploring the potential of lead-chalcogenide monolayers for room-temperature thermoelectric applications. Ceram Int 47(3):3380–3388. https://doi.org/10.1016/j.ceramint.2020.09.183

[39] Sun J, Zhang Y, Fan Y, Tang X, Tan G (2022) Strategies for boosting thermoelectric performance of PbSe: a review. Chem Eng J 431(P4):1–14. https://doi.org/10.1016/j.cej.2021.133699

[40] Rojas-Chávez H, Díaz-de la Torre S, Jaramillo-Vigueras D, Plascencia G (2009) PbTe mechanosynthesis from PbO and Te. J Alloys Compd 483(1–2):275–278. https://doi.org/10.1016/j.jallcom.2008.07.202

[41] Kullerud G (1969) The lead-sulfur system. Am J Sci 267:233–256

[42] Dughaish ZH (2002) Lead telluride as a thermoelectric material for thermoelectric power generation. Physica B Condens Matter 322(1–2):205–223. https://doi.org/10.1016/S0921-4526(02)01187-0

[43] Pei Y, Lalonde A, Iwanaga S, Snyder GJ (2011) High thermoelectric figure of merit in heavy hole dominated PbTe. Energy Environ Sci 4(6):2085–2089. https://doi.org/10.1039/c0ee00456a

[44] Kanatzidis MG (2010) Nanostructured thermoelectrics: the new paradigm? Chem Mater 22(3):648–659. https://doi.org/10.1021/cm902195j

[45] Lucovsky G, White RM (1973) Effects of resonance bonding on the properties of crystalline and amorphous semiconductors. Phys Rev B 8(2):660–667. https://doi.org/10.1103/PhysRevB.8.660

[46] Bencherif Y, Boukra A, Zaoui A, Ferhat M (2011) High-pressure phases of lead chalcogenides. Mater Chem Phys 126(3):707–710. https://doi.org/10.1016/j.matchemphys.2010.12.056

[47] Rousse G et al (2005) Structure of the intermediate phase of PbTe at high pressure. Phys Rev B Condens Matter Mater Phys 71(22):1–6. https://doi.org/10.1103/PhysRevB.71.224116

[48] Fujii Y, Kitamura K, Onodera A, Yamada Y (1984) A new high-pressure phase of PbTe above 16 GPa. Solid State Commun 49(2):135–139. https://doi.org/10.1016/0038-1098(84)90780-4

[49] Ahuja R (2003) High pressure structural phase transitions in IV-VI semiconductors. Phys Status Solidi B Basic Res 235(2):341–347. https://doi.org/10.1002/pssb.200301583

[50] Semonin OE, Luther JM, Beard MC (2012) Quantum dots for next-generation photovoltaics. Mater Today 15(11):508–515. https://doi.org/10.1016/S1369-7021(12)70220-1

[51] Androulakis J, Todorov I, He J, Chung D, Dravid V, Kanatzidis M (2011) Thermoelectrics from abundant chemical elements. J Am Ceram Soc 133:10920–10927

[52] Chattopadhyay T, Werner A, von Schenering HG (1984) Pressure induced phase transition in Iv-Vi compounds. Mater Res Soc Symp Proc 22:93–96

[53] Ponosov YS, Ovsyannikov SV, Streltsov SV, Shchennikov VV, Syassen K (2009) A Raman study of high-pressure phases of lead chalcogenides PbX (X= S, Se, Te). High Pressure Res 29(2):224–229. https://doi.org/10.1080/08957950802604787

[54] Ovsyannikov SV et al (2007) High-pressure X-ray diffraction study of ternary and non-stoichiometric PbTe and PbSe crystals. Physica Status Solidi (b) 244(1):279–284. https://doi.org/10.1002/pssb.200672565

[55] Sadovnikov SI, Gusev AI, Rempel AA (2016) Nanostructured lead sulfide: synthesis, structure and properties. Russ Chem Rev 85(7):731–758. https://doi.org/10.1070/rcr4594

[56] Wang H, Schechtel E, Pei Y, Snyder GJ (2013) High thermoelectric effi ciency of n-type PbS. Adv Energy Mater 3(4):488–495. https://doi.org/10.1002/aenm.201200683

[57] Sadovnikov SI, Gusev AI (2013) Structure and properties of PbS films. J Alloys Compd 573:65–75. https://doi.org/10.1016/j.jallcom.2013.03.290

[58] Jiang JZ, Gerward L, Secco R, Frost D, Olsen JS, Truckenbrodt J (2000) Phase transformation and conductivity in nanocrystal PbS under pressure. J Appl Phys 87(5):2658–2660. https://doi.org/10.1063/1.372235

[59] G. R. O. W. T. H. O. F. Lead, "Mat. Res. Bull. Vol. I0, pp. 277–280, 1975. in the United States. Pergamon Press, Inc. Printed," vol. I, no. 4, pp. 277–280, 1975

[60] Ibáñez M et al (2016) High-performance thermoelectric nanocomposites from nanocrystal building blocks. Nature Commun 7(1):1–7. https://doi.org/10.1038/ncomms10766

[61] Pol BS, Tonejc A, A-plent BGRE, Ka BCL (1979) Crystal data 2. ln$_2$Se$_3$, pp 416–420

[62] Luu SDN et al (2020) Origin of low thermal conductivity in In$_4$Se$_3$. ACS Appl Energy Mater 3(12):12549–12556. https://doi.org/10.1021/acsaem.0c02489

[63] Küpers M et al (2018) Controlled crystal growth of indium selenide, In$_2$Se$_3$, and the crystal structures of α-In$_2$Se$_3$. Inorg Chem 57(18):11775–11781. https://doi.org/10.1021/acs.inorgchem.8b01950

[64] Nasr TB, Abdallah HB, Bennaceur R (2010) First-principles study of the electronic and the optical properties of In6Se7 compound. Physica B: Condens Matter 405(16):3427–3432. https://doi.org/10.1016/j.physb.2010.05.017

[65] Hogg JHC, Sutherland HH, Williams DJ (1973) The crystal structure of tetraindium triselenide. Acta Crystallogr Sect B: Struct Crystallogr Cryst Chem 29(8):1590–1593

[66] Rhyee JS et al (2009) Peierls distortion as a route to high thermoelectric performance in In 4Se3-) crystals. Nature 459(7249):965–968. https://doi.org/10.1038/nature08088

[67] Inoue S, Yoshida T, Morita T (1982) Crystal structure of inse grown from melt and its structure transition. Jpn J Appl Phys 21(2):242–248. https://doi.org/10.1143/JJAP.21.242

[68] Rigoult J, Rimsky A, Kuhn A (1980) Refinement of the 3R γ-indium monoselenide structure type. Acta Crystallog Sect B: Struct Crystallogr Cryst Chem 36(4):916–918

[69] Levy-Clement C, Rioux J, Dahn JR, McKinnon WR (1984) In-situ X-ray characterisation of the reaction of lithium with InSe. Mater Res Bull 19(12):1629–1634. https://doi.org/10.1016/0025-5408(84)90239-3

[70] Hogg JHC (1971) The crystal structure of In6Se7. Acta Crystallogr B 27(8):1630–1634. https://doi.org/10.1107/s056774087100445x

[71] Mori S (1973) Electrical properties of In$_6$Se$_7$. J Phys Soc Jpn 35(1):310. https://doi.org/10.1143/JPSJ.35.310

[72] Cui J, Liu X, Zhang X, Li Y, Deng Y (2011) Bandgap reduction responsible for the improved thermoelectric performance of bulk polycrystalline In$_{2-x}$Cu$_x$Se$_3$ (x = 0–0.2). J Appl Phys 110(2):1–5. https://doi.org/10.1063/1.3609067

[73] Cui J, Peng H, Song Z, Du Z, Chao Y, Chen G (2017) Significantly enhanced thermoelectric performance of γ-In$_2$Se$_3$ through lithiation via chemical diffusion. Chem Mater 29(17):7467–7474. https://doi.org/10.1021/acs.chemmater.7b02467

[74] Klemm W, Hans HU (1934) Messungen an Gallium- und Indium-Verbindungen. X. Über die Chalkogenide von Gallium und Indium. Z Anorg Allg Chem 219(1):45–64. https://doi.org/10.1002/zaac.19342190106

[75] Vilaplana R et al (2018) Experimental and theoretical studies on α-In$_2$Se$_3$ at high pressure. Inorg Chem 57(14):8241–8252. https://doi.org/10.1021/acs.inorgchem.8b00778

[76] Jana MK, Pal K, Waghmare UV, Biswas K (2016) The origin of ultralow thermal conductivity in InTe: lone-pair-induced anharmonic rattling. Angew Chem Int Edn 55(27):7792–7796. https://doi.org/10.1002/ange.201511737

[77] Hogg JHC, Sutherland HH (1973) The crystal structure of tetraindium tritelluride. Acta Crystallogr Sect B: Struct Crystallogr Cryst Chem 29(11):2483–2487

[78] Grochowski EG, Mason DR, Schmitt GA, Smith PH (1964) The phase diagram for the binary system indium-tellurium and electrical properties of In3Te5. J Phys Chem Solids 25(6):551–558. https://doi.org/10.1016/0022-3697(64)90143-X

[79] Debbichi L, Eriksson O, Lebègue S (2014) Electronic structure of In3Se4 and In$_3$Te$_4$ monolayers from ab-initio calculations. Ann Phys 526(9–10):402–407. https://doi.org/10.1002/andp.201400159

[80] Vora-ud A, Thanachayanont C, Jugsujinda S, Amornkitbamrung V, Seetawana T (2011) Study on electronic structure of β-In$_2$Te$_3$ thermoelectric materialfor alternative energy. Procedia Eng 8:2–7. https://doi.org/10.1016/j.proeng.2011.03.001

[81] Zhou Y, Wang W, Li L, Gong P, Tang D (2021) In-plane anisotropic Raman response of layered In$_2$Te$_5$ semiconductor. Appl Phys Lett 118(18):1–5. https://doi.org/10.1063/5.0043547

[82] Chattopadhyay T, Santandrea RP, von Schnering HG (1985) Temperature and pressure dependence of the crystal structure of InTe: A new high pressure phase of InTe. J Phys Chem Solids 46(3):351–356. https://doi.org/10.1016/0022-3697(85)90178-7

[83] Han G et al (2014) A new crystal: layer-structured rhombohedral In3Se4. CrystEngComm 16(3):393–398. https://doi.org/10.1039/c3ce41815d

[84] Lavut EG, Chelovskaya NV, Paukar GQ, Demin VN, Zlomanov VP (1997) The standard molar enthalpy of formation of indium telluride In$_2$Te$_5$. J Chem Thermodyn 29(7):811–815. https://doi.org/10.1006/jcht.1997.0209

[85] Bleris GL, Karakostas T, Stoemenos J, Economou NA (1976) On the short-range order arrangement at the transition state of β-In$_2$Te$_3$. Physica Status Solidi (a) 34(1):243–254. https://doi.org/10.1002/pssa.2210340121

[86] Nassary MM, Dongal M, Gerges MK, Sebage MA (2003) Study of the electrical conductivity and thermoelectric power of In$_2$Te$_5$ single crystals. Physica Status Solidi A Appl Res 199(3):464–470. https://doi.org/10.1002/pssa.200306657

[87] Kushwaha P et al (2014) Physical, optical and nonlinear properties of InS single crystal. Opt Mater 36(3):616–620. https://doi.org/10.1016/j.optmat.2013.10.046

[88] Zavrazhnov AY, Kosyakov AV, Naumov AV, Sergeeva AV, Berezin SS (2013) Study of the In-S phase diagram using spectrophotometric characterization of equilibria between hydrogen and indium sulfides. Thermochim Acta 566:169–174. https://doi.org/10.1016/j.tca.2013.05.031

[89] Ghorbani E, Erhart P, Albe K (2019) Energy level alignment of Cu(In, Ga)(S, Se)$_2$ absorber compounds with In$_2$S$_3$, NaIn$_5$S$_8$, and CuIn$_5$S$_8$ Cd-free buffer materials. Phys Rev Mater 3(7):1–7. https://doi.org/10.1103/PhysRevMaterials.3.075401

[90] Pistor P et al (2016) Structure reinvestigation of α-, β- and γ-In2S3. Acta Crystallogr B Struct Sci Cryst Eng Mater 72(3):410–415. https://doi.org/10.1107/S2052520616007058

[91] Li S, Li X, Ren Z, Zhang Q (2018) Recent progress towards high performance of tin chalcogenide thermoelectric materials. J Mater Chem A Mater 6(6):2432–2448. https://doi.org/10.1039/c7ta09941j

[92] Li Y, He B, Heremans JP, Zhao JC (2016) High-temperature oxidation behavior of thermoelectric SnSe. J Alloys Compd 669:224–231. https://doi.org/10.1016/j.jallcom.2016.01.258

[93] Li Y, Shi X, Ren D, Chen J, Chen L (2015) Investigation of the anisotropic thermoelectric properties of oriented polycrystalline SnSe. Energies 8(7):6275–6285. https://doi.org/10.3390/en8076275

[94] Kumar M, Rani S, Singh Y, Gour KS, Singh VN (2021) Tin-selenide as a futuristic material: properties and applications. RSC Adv 11(12):6477–6503. https://doi.org/10.1039/d0ra09807h

[95] Pham AT et al (2020) High-quality SnSe2 single crystals: electronic and thermoelectric properties. ACS Appl Energy Mater 3:10787–10792

[96] Achimovičová M et al (2011) Structural and morphological study of mechanochemically synthesized tin diselenide. J Mater Chem 21(16):5873–5876. https://doi.org/10.1039/c1jm10330j

[97] Banik A, Shenoy US, Anand S, Waghmare UV, Biswas K (2015) Mg alloying in SnTe facilitates valence band convergence and optimizes thermoelectric properties. Chem Mater 27(2):581–587. https://doi.org/10.1021/cm504112m

[98] Ahmad S et al (2020) Remarkable improvement of thermoelectric figure-of-merit in SnTe through in situ-created Te Nanoinclusions. ACS Appl Energy Mater 3(7):7113–7120. https://doi.org/10.1021/acsaem.0c01156

[99] Ortix C (2021) Nonlinear Hall effect with time-reversal symmetry: theory and material realizations. Adv Quantum Technol 4(9):1–20. https://doi.org/10.1002/qute.202100056

[100] Kannaujiya RM, Khimani AJ, Chaki SH, Chauhan SM, Hirpara AB, Deshpande MP (2020) Growth and characterizations of tin telluride (SnTe) single crystals. Eur Phys J Plus 135(1):1–12. https://doi.org/10.1140/epjp/s13360-019-00022-1

[101] "ilar to that described by Hall (3). The apparatus was calibrated with the fol-," vol. 154, no. 1956, p. 1963, 1963.

[102] Wang L et al (2017) Thermoelectric performance of Se/Cd codoped SnTe via microwave solvothermal method. ACS Appl Mater Interfaces 9(27):22612–22619. https://doi.org/10.1021/acsami.7b06083

[103] Banai RE, Horn MW, Brownson JRS (2016) A review of tin (II) monosulfide and its potential as a photovoltaic absorber. Sol Energy Mater Sol Cells 150:112–129. https://doi.org/10.1016/j.solmat.2015.12.001

[104] Skelton JM, Burton LA, Jackson AJ, Oba F, Parker SC, Walsh A (2017) Lattice dynamics of the tin sulphides SnS2, SnS and Sn2S3: Vibrational spectra and thermal transport. Phys Chem Chem Phys 19(19):12452–12465. https://doi.org/10.1039/c7cp01680h

[105] Koteeswara Reddy N, Devika M, Gopal ESR (2015) Review on tin (II) sulfide (SnS) material: synthesis, properties, and applications. Crit Rev Solid State Mater Sci 40(6):359–398. https://doi.org/10.1080/10408436.2015.1053601

[106] Prasad KG, Kannam SK, Sathian SP (2019) Tunable thermoelectric properties of SnS2 under high pressure at room temperature. Physica B Condens Matter 556:97–102. https://doi.org/10.1016/j.physb.2018.12.004

[107] Zhang L, Dong X, Wang Y, Zheng N, Ma H, Zhang X (2022) One-pot synthesis of SnS2/In2S3 heterostructures for efficient photocatalysis. Appl Surface Sci 579:1–12. https://doi.org/10.1016/j.apsusc.2021.152088

[108] Bletskan MM, Bletskan DI (2014) Electronic structure of Sn2S3 compound with the mixed valency of tin. J Optoelectron Adv Mater 16(5–6):659–664

[109] Gamal GA, Abouzied MA, Sanaa MF (2012) Semiconducting properties of In3Te4 crystals: an experimental study. Turk J Phys 36(1):31–38. https://doi.org/10.3906/fiz-1102-12

[110] Osamura K, Murakami Y, Tomiie Y (1966) Crystal structures of α-and β-Indium Selenide, In2Se3. J Phys Soc Jpn 21(9):1848. https://doi.org/10.1143/JPSJ.21.1848

[111] Lutz HD, Fischer M, Baldus HP, Blachnik R (1988) Zur polymorphie des In2Se3. J Less-Common Metals 143(1–2):83–92. https://doi.org/10.1016/0022-5088(88)90033-1

[112] Siegen U (1995) In4Se3: Neubestimmung. vol. 3, pp. 342–347

[113] Walther R, Deiseroth HJ (1995) Redetermination of the crystal structure of hexaindium heptaselenide, In6Se7. Zeit Kristallogr New Crystal Struct 210(5):359. https://doi.org/10.1524/zkri.1995.210.5.359

[114] Chen ZG, Hana G, Yanga L, Cheng L, Zou J (2012) Nanostructured thermoelectric materials: current research and future challenge. Progress Nat Sci: Mater Int 22(6):535–549. https://doi.org/10.1016/j.pnsc.2012.11.011

[115] Wei J et al (2020) Review of current high-ZT thermoelectric materials. J Mater Sci 55(27):12642–12704. https://doi.org/10.1007/s10853-020-04949-0

[116] Yang L, Chen ZG, Dargusch MS, Zou J (2018) High performance thermoelectric materials: progress and their applications. Adv Energy Mater 8(6):1–28. https://doi.org/10.1002/aenm.201701797

[117] Asfandiyar et al (2017) Thermoelectric SnS and SnS-SnSe solid solutions prepared by mechanical alloying and spark plasma sintering: Anisotropic thermoelectric properties. Sci Rep 7:1–7. https://doi.org/10.1038/srep43262

[118] Duong AT et al (2016) Achieving ZT = 2.2 with Bi-doped n-type SnSe single crystals. Nat Commun 7:1–6. https://doi.org/10.1038/ncomms13713

[119] Parker D, Singh DJ (2010) High-temperature thermoelectric performance of heavily doped PbSe. Phys Rev B Condens Matter Mater Phys 82(3):1–5. https://doi.org/10.1103/PhysRevB.82.035204

[120] Wang H, Pei Y, Lalonde AD, Snyder GJ (2011) Heavily doped p-type PbSe with high thermoelectric performance: an alternative for PbTe. Adv Mater 23(11):1366–1370. https://doi.org/10.1002/adma.201004200

[121] Zhang Q et al (2013) High thermoelectric performance by resonant dopant indium in nanostructured SnTe. Proc Natl Acad Sci U S A 110(33):13261–13266. https://doi.org/10.1073/pnas.1305735110

[122] Zhou B et al (2017) Thermoelectric properties of SnS with na-doping. ACS Appl Mater Interfaces 9(39):34033–34041. https://doi.org/10.1021/acsami.7b08770

[123] Rhyee JS, Ahn K, Lee KH, Ji HS, Shim JH (2011) Enhancement of the thermoelectric figure-of-merit in a wide temperature range in In4Se3−xCl0.03 bulk crystals. Adv Mater 23(19):2191–2194. https://doi.org/10.1002/adma.201004739

[124] Zhu H, Wang G, Wang G, Zhou X, Lu X (2021) The role of electronic affinity for dopants in thermoelectric transport properties of InTe. J Alloys Compd 869:1–6. https://doi.org/10.1016/j.jallcom.2021.159224

[125] Zhang J, Tse K, Wong M, Zhang Y, Zhu J (2016) A brief review of co-doping. Front Phys 11(6):1–21. https://doi.org/10.1007/s11467-016-0577-2

[126] Shenoy US, Bhat DK (2020) Bi and Zn co-doped SnTe thermoelectrics: Interplay of resonance levels and heavy hole band dominance leading to enhanced performance and a record high room temperature: ZT. J Mater Chem C Mater 8(6):2036–2042. https://doi.org/10.1039/c9tc06490g

[127] Fan H et al (2015) Enhanced thermoelectric performance of PbSe co-doped with Ag and Sb. J Alloys Compd 639:106–110. https://doi.org/10.1016/j.jallcom.2015.03.117

[128] Shenoy US, Bhat DK (2022) Selective co-doping improves the thermoelectric performance of SnTe: an outcome of electronic structure engineering. J Alloys Compd 892:1–7. https://doi.org/10.1016/j.jallcom.2021.162221

[129] Androulakis J et al (2010) Thermoelectric enhancement in PbTe with K or Na codoping from tuning the interaction of the light- and heavy-hole valence bands. Phys Rev B Condens Matter Mater Phys 82(11):1–8. https://doi.org/10.1103/PhysRevB.82.115209

[130] Yu B et al (2010) Thermoelectric property studies on thallium-doped lead telluride prepared by ball milling and hot pressing. J Appl Phys 108(1):108–111. https://doi.org/10.1063/1.3452323

[131] Zhang Q et al (2012) Enhancement of thermoelectric figure-of-merit by resonant states of aluminium doping in lead selenide. Energy Environ Sci 5(1):5246–5251. https://doi.org/10.1039/c1ee02465e

[132] Androulakis J, Lee Y, Todorov I, Chung DY, Kanatzidis M (2011) High-temperature thermoelectric properties of n-type PbSe doped with Ga, In, and Pb. Phys Rev B Condens Matter Mater Phys 83(19):1–9. https://doi.org/10.1103/PhysRevB.83.195209

[133] Li JC, Li D, Qin XY, Zhang J (2017) Enhanced thermoelectric performance of p-type SnSe doped with Zn. Scr Mater 126:6–10. https://doi.org/10.1016/j.scriptamat.2016.08.009

[134] Zhang Q et al (2015) Studies on thermoelectric properties of n-type polycrystalline $SnSe_{1-x}S_x$ by iodine doping. Adv Energy Mater 5(12):1–8. https://doi.org/10.1002/aenm.201500360

[135] Li S et al (2018) Heavy doping by bromine to improve the thermoelectric properties of n-type polycrystalline SnSe. Advanced Science 5(9):6–11. https://doi.org/10.1002/advs.201800598

[136] Gong Y et al (2018) Extremely low thermal conductivity and enhanced thermoelectric performance of polycrystalline SnSe by Cu doping. Scr Mater 147:74–78. https://doi.org/10.1016/j.scriptamat.2017.12.035

[137] Zhao LD et al (2016) Enhanced thermoelectric properties in the counter-doped SnTe system with strained endotaxial SrTe. J Am Chem Soc 138(7):2366–2373. https://doi.org/10.1021/jacs.5b13276

[138] Wu H et al (2018) Sodium-doped tin sulfide single crystal: a nontoxic earth-abundant material with high thermoelectric performance. Adv Energy Mater 8(20):1–8. https://doi.org/10.1002/aenm.201800087

[139] Tan Q et al (2014) Thermoelectrics with earth abundant elements: low thermal conductivity and high thermopower in doped SnS. J Mater Chem A Mater 2(41):17302–17306. https://doi.org/10.1039/c4ta04462b

[140] Haleoot R, Hamad B (2020) Thermoelectric properties of doped β-InSe by Bi: First principle calculations. Phys B Condens Matter 587:1–5. https://doi.org/10.1016/j.physb.2020.412105

[141] Li G et al (2013) Improvement of thermoelectric properties of in 4 Se 3 bulk materials with Cu nanoinclusions. J Am Ceram Soc 96(9):2703–2705. https://doi.org/10.1111/jace.12518

[142] Schmitz A, de Boor J, Mull K, Müller E (2016) Tailoring the mechanical properties of thermoelectric lead telluride by alloying with non-doping calcium. J Mater Sci 51(14):6933–6943. https://doi.org/10.1007/s10853-016-9980-x

[143] Esparza R, Perez R, Rosas G, Universitaria C (2010) Mater. Res. Soc. Symp. Proc. Vol. 1242 © 2010 Materials Research Society vol 1242, pp 1–6

[144] Li F et al (2017) Optimization of thermoelectric properties of n-type Ti, Pb co-doped SnSe. Inorg Chem Front 4(10):1721–1729. https://doi.org/10.1039/c7qi00436b

[145] Li C et al (2020) High thermoelectric performance of co-doped P-type polycrystalline SnSe via optimizing electrical transport properties. ACS Appl Mater Interfaces 12(7):8446–8455. https://doi.org/10.1021/acsami.9b20610

[146] Wang H et al (2018) Optimization of peak and average figures of merits for in & Se co-doped SnTe alloys. Inorg Chem Front 5(4):793–801. https://doi.org/10.1039/c7qi00781g

[147] Kihoi SK, Shenoy US, Kahiu JN, Kim H, Bhat DK, Lee HS (2023) Pushing the limit of synergy in SnTe-based thermoelectric materials leading to an ultra-low lattice thermal conductivity and enhanced ZT. Sustain Energy Fuels 7(8):1916–1929. https://doi.org/10.1039/d3se00068k

[148] Lin ZS, Chen L, Wang LM, Zhao JT, Wu LM (2013) A promising mid-temperature thermoelectric material candidate: Pb/Sn-codoped $In_4Pb_xSn_ySe_3$. Adv Mater 25(34):4800–4806. https://doi.org/10.1002/adma.201302038

[149] Pei Y, LaLonde AD, Heinz NA, Snyder GJ (2012) High thermoelectric figure of merit in PbTe alloys demonstrated in PbTe-CdTe. Adv Energy Mater 2(6):670–675. https://doi.org/10.1002/aenm.201100770

[150] Wu Y et al (2020) Thermoelectric enhancements in PbTe alloys due to dislocation-induced strains and converged bands. Adv Sci 7(12):1–9. https://doi.org/10.1002/advs.201902628

[151] Wei TR et al (2017) Thermoelectric transport properties of polycrystalline SnSe alloyed with PbSe. Appl Phys Lett 110(5):1–5. https://doi.org/10.1063/1.4975603

[152] Li W et al (2015) Band and scattering tuning for high performance thermoelectric Sn1−xMnxTe alloys. Journal of Materiomics 1(4):307–315. https://doi.org/10.1016/j.jmat.2015.09.001

[153] Zhu Y et al (2022) Multiple valence bands convergence and strong phonon scattering lead to high thermoelectric performance in p-type PbSe. Nat Commun 13(1):1–9. https://doi.org/10.1038/s41467-022-31939-4

[154] Zhao L et al (2021) Enhanced thermoelectric properties of n-type Cl doped PbS-based materials via Bi alloying. J Alloys Compd 859:1–7. https://doi.org/10.1016/j.jallcom.2020.157788

[155] Qian X et al (2019) Synergistically optimizing interdependent thermoelectric parameters of n-type PbSe through alloying CdSe. Energy Environ Sci 12(6):1969–1978. https://doi.org/10.1039/c8ee03386b

[156] Zeng L et al (2016) Enhanced thermoelectric performance in PbSe-SrSe solid solution by Mn substitution. J Alloys Compd 687:765–772. https://doi.org/10.1016/j.jallcom.2016.06.172

[157] Zhao Q, Wang D, Qin B, Wang G, Qiu Y, Zhao LD (2019) Synergistically optimized electrical and thermal transport properties of polycrystalline SnSe via alloying SnS. J Solid State Chem 273:85–91. https://doi.org/10.1016/j.jssc.2019.02.038

[158] He J, Girard SN, Kanatzidis MG, Dravid VP (2010) Microstructure-lattice thermal conductivity correlation in nanostructured $PbTe_{0.7}S_{0.3}$ thermoelectric materials. Adv Funct Mater 20(5):764–772. https://doi.org/10.1002/adfm.200901905

[159] Aksamija Z (2015) Lattice thermal transport in si-based nanocomposites for thermoelectric applications. J Electron Mater 44(6):1644–1650. https://doi.org/10.1007/s11664-014-3505-7

[160] Harman TC, Taylor PJ, Walsh MP, LaForge BE (2002) Quantum dot superlattice thermoelectric materials and devices. Science 297(5590):2229–2232. https://doi.org/10.1126/science.1072886

[161] Rogacheva EI, Nashchekina ON, Meriuts AV, Lyubchenko SG, Dresselhaus MS, Dresselhaus G (2005) Quantum size effects in n-PbTe/ p-SnTe/ n-PbTe heterostructures. Appl Phys Lett 86(6):1–3. https://doi.org/10.1063/1.1862338

[162] Hsin CL, Huang CW, Wu MH, Cheng SY, Pan RC (2019) Synthesis and thermoelectric properties of indium telluride nanowires. Mater Res Bull 112:61–65. https://doi.org/10.1016/j.materresbull.2018.12.006

[163] Ju H, Kim J (2020) Anion-exchanged porous SnTe nanosheets for ultra-low thermal conductivity and high-performance thermoelectrics. Chem Eng J 402:1–7. https://doi.org/10.1016/j.cej.2020.126274

[164] Li Z et al (2016) Systhesizing SnTe nanocrystals leading to thermoelectric performance enhancement via an ultra-fast microwave hydrothermal method. Nano Energy 28:78–86. https://doi.org/10.1016/j.nanoen.2016.08.008

[165] Johnsen S et al (2011) Nanostructures boost the thermoelectric performance of PbS. J Am Chem Soc 133(10):3460–3470. https://doi.org/10.1021/ja109138p

[166] Huang Y, Yuan H, Chen H (2022) High thermoelectric performance of two-dimensional layered AB2Te4 (A = Sn, Pb; B = Sb, Bi) ternary compounds. Phys Chem Chem Phys 25(3):1808–1818. https://doi.org/10.1039/d2cp05258j

[167] Xu R et al (2019) Nanostructured SnSe integrated with Se quantum dots with ultrahigh power factor and thermoelectric performance from magnetic field-assisted hydrothermal synthesis. J Mater Chem A Mater 7(26):15757–15765. https://doi.org/10.1039/c9ta03967h

[168] Ju H, Park D, Kim J (2019) Fabrication of porous SnS nanosheets and their combination with conductive polymer for hybrid thermoelectric application. Chem Eng J 356:950–954. https://doi.org/10.1016/j.cej.2018.09.106

[169] Li Z et al (2017) Surface oxidation and thermoelectric properties of indium-doped tin telluride nanowires. Nanoscale 9(35):13014–13024. https://doi.org/10.1039/c7nr04934j

[170] Li MS, Chen KX, Mo DC, Lyu SS (2019) Predicted high thermoelectric performance in a two-dimensional indium telluride monolayer and its dependence on strain. Phys Chem Chem Phys 21(44):24695–24701. https://doi.org/10.1039/c9cp04666f

[171] Dresselhaus MS et al (2007) New directions for low-dimensional thermoelectric materials. Adv Mater 19(8):1043–1053. https://doi.org/10.1002/adma.200600527

[172] Omanović-Mikličanin E, Badnjević A, Kazlagić A, Hajlovac M (2020) Nanocomposites: a brief review. Health Technol 10:51–59

[173] Ibanez M, Zamani R, Gorsse S, Fan J, Ortega S, Cadavid D, Morante JR, Arbiol J, Cabot A (2013) Core–shell nanoparticles as building blocks for the bottom-up production of functional nanocomposites: PbTe–PbS thermoelectric properties. ACS Nano 7(3):2573–2586

[174] Yim JH et al (2012) Thermoelectric properties of indium-selenium nanocomposites prepared by mechanical alloying and spark plasma sintering. J Electron Mater 41(6):1354–1359. https://doi.org/10.1007/s11664-012-1940-x

[175] Huang L et al (2020) Facile: In situ solution synthesis of SnSe/rGO nanocomposites with enhanced thermoelectric performance. J Mater Chem A Mater 8(3):1394–1402. https://doi.org/10.1039/c9ta11737g

[176] Zhou NN, Hu ZQ, Nasser R, Song JM (2021) Thermoelectric properties of PbSe nanocomposites from solution-processed building blocks. ACS Appl Energy Mater 4(2):2014–2019.

[177] Jiang Z et al (2020) Achieving High Thermoelectric Performance in p-Type BST/PbSe Nanocomposites through the Scattering Engineering Strategy. ACS Appl Mater Interfaces. https://doi.org/10.1021/acsami.0c13542

[178] Wang H et al (2015) High thermoelectric performance of a heterogeneous PbTe nanocomposite. Chem Mater 27(3):944–949. https://doi.org/10.1021/cm5042138

[179] Dong J, Liu W, Li H, Su X, Tang X, Uher C (2013) In situ synthesis and thermoelectric properties of PbTe-graphene nanocomposites by utilizing a facile and novel wet chemical method. J Mater Chem A Mater 1(40):12503–12511. https://doi.org/10.1039/c3ta12494k

[180] Zhao Y, Maurya D, Miner A, Khodaparast GA, Priya S (2015) Enhanced thermoelectric performance in PbTe–PbS nanocomposites. Energy Harvesting and Systems 2(1–2):55–62. https://doi.org/10.1515/ehs-2015-0004

[181] Girard SN et al (2010) In situ nanostructure generation and evolution within a bulk thermoelectric material to reduce lattice thermal conductivity. Nano Lett 10(8):2825–2831. https://doi.org/10.1021/nl100743q

[182] Sootsman JR et al (2010) Microstructure and thermoelectric properties of mechanically robust PbTe-Si eutectic composites. Chem Mater 22(3):869–875. https://doi.org/10.1021/cm9016672

[183] Feng D, Chen YX, Fu LW, Li J, He JQ (2018) SnSe + Ag2Se composite engineering with ball milling for enhanced thermoelectric performance. Rare Met 37(4):333–342. https://doi.org/10.1007/s12598-017-0994-6

[184] Shu Y et al (2018) Modification of Bulk Heterojunction and Cl Doping for High-Performance Thermoelectric SnSe2/SnSe Nanocomposites. ACS Appl Mater Interfaces 10(18):15793–15802. https://doi.org/10.1021/acsami.8b00524

[185] Chotia C, Tarachand Y, Okram GS, Kuo YK, Hussain S (2021) Enhanced thermoelectric properties of (SnS)$_{1-x}$(SnO)$_x$: $x \leq$ 10.79% nanocomposites prepared by polyol method. J Mater Sci: Mater Electron 32:10702–10711. https://doi.org/10.1007/s10854-021-05727-7

[186] Jiang Q et al (2020) High thermoelectric performance in SnTe nanocomposites with all-scale hierarchical structures. ACS Appl Mater Interfaces 12(20):23102–23109. https://doi.org/10.1021/acsami.0c03349

[187] Li D et al (2016) Enhanced thermoelectric performance in SnSe based composites with PbTe nanoinclusions. Energy 116:861–866. https://doi.org/10.1016/j.energy.2016.10.023

[188] Hwang J et al (2021) Enhancement of thermoelectric performance in a non-toxic CuInTe2/SnTe coated grain nanocomposite. J Mater Chem A Mater 9(26):14851–14858. https://doi.org/10.1039/d1ta02893f

[189] Chang C, Ibáñez M (2021) Enhanced thermoelectric performance by surface engineering in SnTe-PbS nanocomposites. Materials 14(18):1–9. https://doi.org/10.3390/ma14185416

[190] Ahmad S et al (2020) Band convergence and phonon scattering mediated improved thermoelectric performance of SnTe-PbTe nanocomposites. ACS Appl Energy Mater 3(9):8882–8891. https://doi.org/10.1021/acsaem.0c01359

[191] Lee MH et al (2013) Thermoelectric properties of SrTiO3 nanoparticles dispersed indium selenide bulk composites. Appl Phys Lett 102(22):1–5. https://doi.org/10.1063/1.4809677

[192] Zhai Y et al (2013) Thermoelectric performance of the ordered In4Se3-in composite constructed by monotectic solidification. J Mater Chem A Mater 1(31):8844–8847. https://doi.org/10.1039/c3ta01599h

[193] Chandra S, Dutta P, Biswas K (2022) High-performance thermoelectrics based on solution-grown SNSE nanostructures. ACS Nano 16(1):7–14. https://doi.org/10.1021/acsnano.1c10584

[194] Banik A, Roychowdhury S, Biswas K (2018) The journey of tin chalcogenides towards high-performance thermoelectrics and topological materials. Chem Commun 54(50):6573–6590. https://doi.org/10.1039/c8cc02230e

[195] Sharma Y, Srivastava P (2012) Electronic, optical and transport properties of α-, β- And γ-phases of spinel indium sulphide: An ab initio study. Mater Chem Phys 135(2–3):385–394. https://doi.org/10.1016/j.matchemphys.2012.04.064

[196] Shi W, Gao M, Wei J, Gao J, Fan C, Ashalley E, Li H, Wang Z (2018) Tin selenide (SnSe): growth, properties, and applications. Adv Sci 5(4):1–22. https://doi.org/10.1002/advs.201700602

[197] Tanwar P, Panwar AK, Singh S, Srivatava AK (2020) Microstructural and optical properties investigation of variable thickness of Tin Telluride thin films. Thin Solid Films 693:1–9. https://doi.org/10.1016/j.tsf.2019.137708

[198] Zhang H, Talapin DV (2014) Thermoelectric tin selenide: The beauty of simplicity. Angew Chem Int Edn 53(35):9126–9127. https://doi.org/10.1002/anie.201405683